Physics of Plasmas

# X-ray continuum as a measure of pressure and fuel–shell mix in compressed isobaric hydrogen implosion cores

Cite as: Phys. Plasmas **22**, 022707 (2015); https://doi.org/10.1063/1.4907667
Submitted: 06 August 2014 . Accepted: 22 January 2015 . Published Online: 12 February 2015

R. Epstein, V. N. Goncharov, F. J. Marshall, R. Betti, R. Nora, A. R. Christopherson, I. E. Golovkin, and J. J. MacFarlane

View Online Export Citation CrossMark

ARTICLES YOU MAY BE INTERESTED IN

Direct-drive inertial confinement fusion: A review
Physics of Plasmas **22**, 110501 (2015); https://doi.org/10.1063/1.4934714

Development of the indirect-drive approach to inertial confinement fusion and the target physics basis for ignition and gain
Physics of Plasmas **2**, 3933 (1995); https://doi.org/10.1063/1.871025

Improving the hot-spot pressure and demonstrating ignition hydrodynamic equivalence in cryogenic deuterium–tritium implosions on OMEGA
Physics of Plasmas **21**, 056315 (2014); https://doi.org/10.1063/1.4876618

© 2015 AIP Publishing LLC.

# X-ray continuum as a measure of pressure and fuel–shell mix in compressed isobaric hydrogen implosion cores

R. Epstein,[1] V. N. Goncharov,[1] F. J. Marshall,[1] R. Betti,[2] R. Nora,[2] A. R. Christopherson,[2] I. E. Golovkin,[3] and J. J. MacFarlane[3]
[1]*Laboratory for Laser Energetics, University of Rochester, Rochester, New York 14623, USA*
[2]*Fusion Science Center and Laboratory for Laser Energetics, University of Rochester, Rochester, New York 14623, USA*
[3]*Prism Computational Sciences, Madison, Wisconsin 53711, USA*

(Received 6 August 2014; accepted 22 January 2015; published online 12 February 2015)

Pressure, by definition, characterizes the conditions within an isobaric implosion core at peak compression [Gus'kov *et al.*, Nucl. Fusion **16**, 957 (1976); Betti *et al.*, Phys. Plasmas **8**, 5257 (2001)] and is a key parameter in quantifying its near-ignition performance [Lawson, Proc. Phys. Soc. London, B **70**, 6 (1957); Betti *et al.*, Phys. Plasmas **17**, 058102 (2010); Goncharov *et al.*, Phys. Plasmas **21**, 056315 (2014); and Glenzer *et al.*, Phys. Plasmas **19**, 056318 (2012)]. At high spectral energy, where the x-ray emission from an imploded hydrogen core is optically thin, the emissivity profile can be inferred from the spatially resolved core emission. This emissivity, which can be modeled accurately under hot-core conditions, is dependent almost entirely on the pressure when measured within a restricted spectral range matched to the temperature range anticipated for the emitting volume. In this way, the hot core pressure at the time of peak emission can be inferred from the measured free-free emissivity profile. The pressure and temperature dependences of the x-ray emissivity and the neutron-production rate explain a simple scaling of the total filtered x-ray emission as a constant power of the total neutron yield for implosions of targets of similar design over a broad range of shell implosion isentropes. This scaling behavior has been seen in implosion simulations and is confirmed by measurements of high-isentrope implosions [Sangster *et al.*, Phys. Plasmas **20**, 056317 (2013)] on the OMEGA laser system [Boehly *et al.*, Opt. Commun. **133**, 495 (1997)]. Attributing the excess emission from less-stable, low-isentrope implosions, above the level expected from this neutron-yield scaling, to the higher emissivity of shell carbon mixed into the implosion's central hot spot, the hot-spot "fuel–shell" mix mass can be inferred. © *2015 AIP Publishing LLC*. [http://dx.doi.org/10.1063/1.4907667]

## I. INTRODUCTION

Measurements of continuum x-ray emission from the central hot spots of inertial confinement fusion (ICF)[1] implosions at stagnation can be directly related to hot-spot conditions using the relatively simple dependence of continuum spectral emission rates on temperature and density or pressure. Since thermonuclear ignition and high energy gain are the goals of ICF,[2,3] one would naturally look to neutron yield as the primary measure of implosion performance. The benchmarks of progress toward ignition, or toward implosion performance that scales to ignition with higher drive energy,[4] however, are specified in terms of core conditions at peak compression.[5] Short of ignition, neutron yield, and x-ray emission measurements can be used in similar ways to infer hot-spot conditions.[6] The current strategy is to achieve high-temperature central hot spots within fuel shells compressed at low entropy to high areal densities. A key measure of near-ignition performance in ICF, through the Lawson criterion,[7] is the hot-spot pressure.[8] Consequently, a direct relationship between the hot-spot pressure and the measured hot-spot x-ray continuum emissivity, based as little as possible on prior assumptions about hot-spot temperature profiles, normalization to simulations, etc., would be very important.

At a sufficiently high spectral energy, typically $h\nu > 3\,\mathrm{keV}$ for cryogenic implosions on the 60-beam OMEGA laser system,[9] the imploded cores are optically thin and the x-ray measurements are a direct measure of the emissivity, free of absorption and other transport effects. With instrument spectral responses narrowed to energies matched to the anticipated temperature of the hot spot, as will be described at the end of Sec. II, the free-free (FF) emissivity[10] of hot-spot hydrogen scales as the square of the hot-spot pressure and is nearly independent of the temperature. The simple pressure dependence of the emissivity, the isobaric state of the hot spot at stagnation,[11,12] and the known temperature–density scaling of the neutron-production rate explain a simple scaling behavior of the x-ray yield as a constant power of the neutron yield over a factor-of-10 range in neutron yield in an ensemble of similar targets imploded with a variety of laser pulses over a broad range of shell isentropes. This is a quantitative prediction based on our understanding of isobaric hot spots that has been confirmed with measured x-ray and neutron yields. In an unstable implosion, a trace amount of shell material (above ~10-ng CH) mixed into the hot spot (~2.1 $\mu$g) can increase the x-ray emission measurably because of the relatively high emissivity per atom of carbon without significantly altering the deuterium and

 © 2015 AIP Publishing LLC

tritium (DT) concentrations that, along with the hot-spot temperature, determine the neutron yield.

Using the x-ray yield expected from the neutron-yield scaling as a point of reference, the excess x-ray emission and the known FF and free-bound (FB) emissivity[10] of carbon provide a measure of this "fuel–shell" mix mass. This mix-mass estimate is similar in some respects to recent measurements of mix mass in National Ignition Facility (NIF)[13] implosions based on the ratio of the x-ray and neutron yields.[14] Earlier measurements[15] of mix mass in NIF implosions were based on the K-shell line emission of M-shell ionization species of higher-$Z$ shell dopants.[16] Dopant line emission indicates mix originating from the doped shell layers only, while carbon continuum emission indicates fuel–shell mix originating from anywhere in the capsule shell.

The pressure profile within an imploded core at the time of peak emission can be obtained from the emissivity profile of the object, and the emissivity profile can be obtained from its projection recorded on an image plane by an imaging device. The fundamental quantity of radiation is the specific intensity $I(\vec{x}, \hat{\Omega}, \nu)$, which is the amount of radiation energy per unit time arriving at a position $\vec{x}$ in space, per unit area within an infinitesimal area element at this point, oriented normal to the propagation direction given by the unit normal vector $\hat{\Omega}$, per unit spectral range within an infinitesimal interval of frequency, centered at the frequency $\nu$, and traveling within an infinitesimal cone of solid angle, per steradian, centered on the direction $\hat{\Omega}$. We will write it as $I_\nu$ for short. The time-independent equation of transfer governing the change $\mathrm{d}I_\nu$ in the specific intensity of radiation propagating an infinitesimal distance $\mathrm{d}s$ along the direction $\hat{\Omega}$ is

$$\frac{\mathrm{d}I_\nu}{\mathrm{d}s} = \frac{\varepsilon_\nu}{4\pi} - \kappa_\nu I_\nu, \tag{1}$$

where the interaction of radiation and matter with each other is described entirely in terms of the plasma emissivity $\varepsilon_\nu$ and the opacity $\kappa_\nu$ of the matter.[17] The emissivity specifies the energy per unit time that is emitted per unit volume isotropically into all directions, within an infinitesimal interval of frequency centered at the frequency $\nu$. The opacity is the fraction of the specific intensity absorbed per unit distance of propagation. We assume that all radiation of interest propagates at the speed of light $c$ without refraction or dispersion and that any photon scattering involving a change of frequency or direction is accounted for effectively by a combination of absorption and emission included in $\varepsilon_\nu$ together with $\kappa_\nu$.

In the optically thin limit, there is only emission and no attenuation, and the solution to the equation of transfer is the path integral

$$I_\nu(\vec{x}) = \int_{-\infty}^{\vec{x}} \frac{\varepsilon_\nu(\vec{r})}{4\pi} \mathrm{d}\vec{s}. \tag{2}$$

The integration variable $\vec{s}$ is a point along a straight-line photon path arriving at a point $\vec{x}$ on the image plane, and $\vec{r}$ is the position of that point on the path relative to an arbitrary fixed point of reference within the emitting object. The integration path is a straight line arriving at the observer position from arbitrarily far away, indicated symbolically as "$-\infty$," but only points along the path within the emission source contribute to the integral. The imaging device selects from the set of all paths $\hat{\Omega}$ ending at any one $\vec{x}$ so that the image represents a useful projection of the emissivity profile. For the purposes of this discussion, we assume that the imaging device records an orthographic projection of the source, such that the direction $\hat{\Omega}$ of all paths is the same. In spherical geometry, Eq. (2) gives the specific intensity as an Abel transform[18] of the emissivity profile. For example, a spherically symmetric emissivity distribution $\varepsilon_\nu(r)$ produces the specific intensity

$$I_\nu(x) = \frac{1}{2\pi} \int_x^\infty \frac{\varepsilon_\nu(r) r}{\sqrt{r^2 - x^2}} \mathrm{d}r, \tag{3}$$

and the emissivity distribution can be recovered from the inverse Abel transform of the imaged intensity,

$$\varepsilon_\nu(r) = -4 \int_r^\infty \frac{\mathrm{d}I_\nu(x)}{\mathrm{d}x} \frac{\mathrm{d}x}{\sqrt{x^2 - r^2}}. \tag{4}$$

The point $x = 0$ on the image plane is the projection of the center of the radial emissivity distribution at $r = 0$, and we assume that all geometrical and optical effects of an actual camera, such as magnification, etc., have already been taken into account.

If the emissivity is a known function of pressure alone, the radial pressure profile of a spherical hot spot can be inferred from the emissivity profile extracted from the imaged intensity using Eq. (4). If, in addition, the hot spot is isobaric, the pressure is constant throughout the hot spot out to its outer radius $R$ and the emissivity will be constant within this radius; we find using Eq. (4) that the intensity profile of its image is elliptical

$$I_\nu(x) = \frac{\varepsilon_\nu(0)}{2\pi} \sqrt{R^2 - x^2}. \tag{5}$$

The integral of the specific intensity given by Eq. (2) over the image plane gives the total emitted power per unit solid angle at the image plane

$$\int I_\nu(\vec{x}) d^2\vec{x} = \int \int_{-\infty}^{\infty} \frac{\varepsilon_\nu(\vec{r})}{4\pi} \mathrm{d}\vec{s} d^2\vec{x} = \frac{1}{4\pi} \int \varepsilon_\nu(\vec{r}) d^3\vec{r}. \tag{6}$$

Assuming the hot spot radiates isotropically, the total spectral power $P_\nu$ is obtained by applying a factor of $4\pi$. In the case of the flat emissivity profile of an isobaric core, this gives

$$P_\nu = \frac{4\pi}{3} R^3 \varepsilon_\nu(0). \tag{7}$$

The isobaric sphere, then, possesses a remarkable simplicity: All quantities pertaining to emission can be described in terms of a single radius and a single emissivity that depends on one parameter—the pressure. In Secs. II–V, departures of

the emissivity from pure pressure dependence, hot spots that are not strictly isobaric, "fuel–shell mix," and other complications will be considered.

## II. PRESSURE DEPENDENCE OF X-RAY EMISSION FROM ISOBARIC HOT SPOTS

The emissivity of an imploded hydrogen hot spot of a cryogenic implosion is almost entirely the result of FF emission from hydrogen. The expression for the FF emissivity of a hot plasma of fully stripped ions at photon frequency $\nu$, temperature $T$, electron and ion densities $n_e$ and $n_i$, respectively, and average nuclear charge squared $\langle Z^2 \rangle$ is

$$\varepsilon_\nu^{FF} = \frac{32}{3}\sqrt{\frac{\pi}{3}}\alpha^3 \chi_H a_0^3 \langle Z^2 \rangle n_e n_i \left(\frac{\chi_H}{kT}\right)^{1/2} g_{FF} e^{-h\nu/kT}, \quad (8)$$

where $\alpha$ is the fine-structure constant, $\alpha \cong 1/137$, $a_0$ is the Bohr radius, and $\chi_H$ is the K-shell ionization energy of hydrogen.[10] The units of this expression are energy per volume, per steradian, per time, and per frequency. Throughout this paper, $T = T_e$ is the electron temperature. Since the hot-spot hydrogen is almost completely ionized, $\langle Z^2 \rangle = 1$, but the $Z$ dependence in Eq. (8) will be kept, anticipating the discussion in Sec. V of the contamination of the hot spot by carbon as the result of fuel–shell mix. As will be shown in Sec. V, the FB contribution to hydrogen emissivity is negligible under hot-spot conditions.

This emissivity is written in a form first obtained in a semiclassical treatment by Kramers.[19] The correction factor $g_{FF}$ accounting for quantum-mechanical effects in FF absorption and emission and also in other absorption and emission processes was introduced by Gaunt.[20] The same Gaunt factor applies to both emission and absorption, a result of the microscopic reversibility of these processes.[21] Many versions of the Gaunt factor have been provided over many years by many authors who, to cite just a few, include correct isolated-ion quantum wave functions,[22] relativistic effects,[23] collective effects,[24] and high-density effects such as electron degeneracy[25] and strong plasma coupling.[26,27] A particularly simple and accurate Gaunt factor for hydrogen has been provided by Kulsrud[28]

$$g_{FF} = \frac{\sqrt{3}}{\pi}\ln\left[\frac{(\beta^2+u)^{1/2}+\beta}{(\beta^2+u)^{1/2}-\beta}\right], \quad (9)$$

where $u = h\nu/kT$ and $\beta^2$ is an average energy parameter

$$\beta^2 = \left\langle \frac{\hbar^2 k^2}{2m_e kT} \right\rangle \quad (10)$$

representing an effective average initial electron energy. Kulsrud finds that the value $\beta = 0.87$ provides a good fit to an earlier, more-accurate quantum result by Sommerfeld.[28] We verify that Eq. (9) is a good approximation to the standard results of Karzas and Latter[22] (KL) in the high-temperature limit $kT \gg \chi_H$, which is the relevant regime for implosion cores at peak conditions. We also verify that the asymptotic expression

$$g_{FF} \approx \frac{2\sqrt{3}}{\pi}\frac{\beta}{u^{1/2}} \quad (11)$$

is a useful approximation to Eq. (9) at high photon energies $h\nu > kT$. This is consistent with the sensitive range of the filtered gated monochromatic x-ray imager (GMXI) camera[29] ($h\nu \sim 5$ keV), described below, and the expected core temperatures ($kT \sim 2$ keV). This is also well into the optically thin spectral range where emission is directly related to the hot-spot emissivity. Using Eq. (11) in Eq. (8) provides an emissivity expression with accurate temperature and photon-energy scaling that will be used in later discussion of the interpretation of measured energy-integrated core emission.

Some brief textbook summaries of FF and FB emission and absorption dismiss the Gaunt factor as a constant correction of order unity,[3] which for our purposes would be a poor approximation. Equation (11) provides a convenient simplification and ensures correct asymptotic scaling behavior. This asymptotic expression for the Kulsrud Gaunt factor is plotted in Fig. 1 along with the result of the full expression, Eq. (9), and KL values.[22] The Kulsrud Gaunt factor depends only on $u = h\nu/kT$, while the KL results also depend on the parameter $\gamma^2 = Z^2\chi_H/kT$. Here, we simply plot the KL values for hydrogen ($Z = 1$) at the temperatures 2 keV and 6 keV to show that the departure of the KL from the Kulsrud values is small and that their temperature dependence at constant $u = h\nu/kT$ can be cautiously disregarded for the purposes of this discussion. The plot range is extended over an order of magnitude to show that the asymptotic behavior of the Kulsrud expression is correct. The relevant range of $h\nu/kT$ for our chosen imaging instrument, the GMXI, with a response function denoted here and in Fig. 1 as "B,"

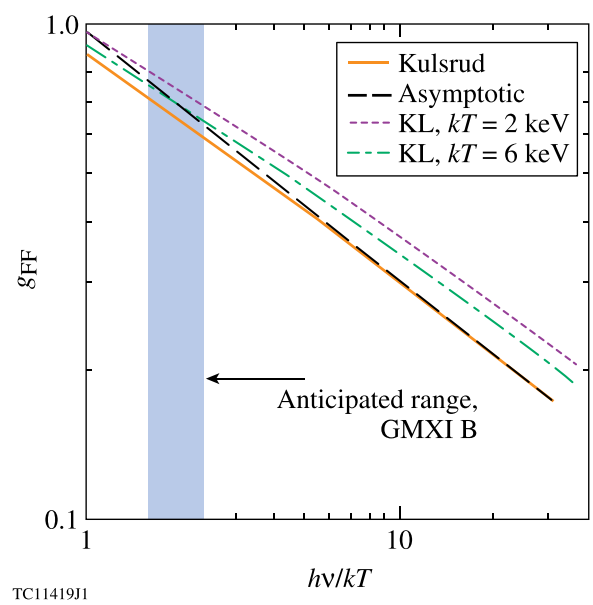


FIG. 1. Plot of the Kulsrud[28] approximation to the hydrogen FF Gaunt factor versus $u = h\nu/kT$ [solid (orange) curve] given by Eq. (9) and its asymptotic approximation given by Eq. (11) [dashed black curve]. KL values for $kT = 2$ and 6 keV are shown for comparison by the dotted (purple) and dashed–dotted (green) curves, respectively. The relevant range of $u$ for the anticipated core conditions and instrumentation (GMXI B) is indicated approximately by the blue shading. The asymptotic behavior of the Kulsrud approximation agrees with that of the KL[22] values.

indicated by the blue-shaded strip. Here, the agreement among the four results is particularly close. The KL and Kulsrud formulations do not consider the effects of relativistic electron motion or the effects of degeneracy and strong coupling on the energy levels of the ions and on the free-electron energy distribution. These effects will not be significant under hot-spot emission conditions, although the latter two effects must be considered in the surrounding, relatively cold compressed shell, particularly earlier in the implosion.[27] Evaluating the numerical coefficient in Eq. (11) gives $g_{\mathrm{H,FF}} \approx 0.959\, u^{-0.5}$, which is very close to $g_{\mathrm{H,FF}} = 0.966\, u^{-0.41}$, a numerical fit to the KL hydrogen FF result near $h\nu \approx 5.39$ keV and $h\nu_0/kT \approx 2$, anticipating the conditions where Eq. (11) will be applied.

Let us specialize to fully ionized hydrogen, where $\langle Z^2 \rangle = 1$ and $n_e = n_i$. We then insert the Kulsrud Gaunt factor given by Eq. (11) into Eq. (8) and obtain

$$\varepsilon_\nu^{\mathrm{FF}} = \frac{64}{3\sqrt{\pi}} \beta \alpha^3 \chi_{\mathrm{H}} a_0^3 n_i^2 \left(\frac{\chi_{\mathrm{H}}}{kT}\right)^{1/2} \left(\frac{kT}{h\nu}\right)^{1/2} e^{-h\nu/kT}. \tag{12}$$

Using the ideal gas equation of state $P = (n_e + n_i)\ kT$ to replace density with pressure, we obtain

$$\varepsilon_\nu^{\mathrm{FF}} = \frac{16}{3\sqrt{\pi}} \beta \alpha^3 \chi_{\mathrm{H}} a_0^3 \left(\frac{P}{kT}\right)^2 \left(\frac{\chi_{\mathrm{H}}}{h\nu}\right)^{1/2} e^{-h\nu/kT}. \tag{13}$$

This ideal gas equation of state is an approximation to the more general expression $P = k(n_e T_e + n_i T_i)$, recognizing that the ion temperature $T_i$ can exceed the electron temperature during the convergence of shocks that forms the hot spot. During peak compression, however, the two temperatures equilibrate rapidly, so $T_i = T_e$—a useful approximation that has been standard in recent discussions of hot-spot dynamics—can be applied here with caution. We will show that this emissivity is almost exclusively a function of pressure when measured with an appropriate spectral response.

Three spectral response channels of the GMXI[29] x ray camera are shown in Fig. 2. These response functions are nearly Gaussian in shape with spectral widths of approximately $\Delta h\nu \approx 1$ keV centered at energies near $h\nu_0 \approx 5$ keV. The three channels, denoted A, B, and C, differ in the 1, 2, and 3-mil thicknesses of Al in their respective filter packages. These response functions are approximated adequately for our purposes by a Gaussian function

$$F(\nu) = F_0 e^{-(\nu-\nu_0)^2/(\Delta\nu)^2} \tag{14}$$

with a transmission width $\Delta\nu$ centered at $\nu_0$. With a response function of the form of Eq. (14), the frequency-integrated emissivity expression obtained using the emissivity given by Eq. (13) is

$$E_{\nu_0,\Delta\nu} = \frac{16}{3\sqrt{\pi}} \alpha^3 \chi_{\mathrm{H}} a_0^3 \beta \left(\frac{P}{kT}\right)^2 \left(\frac{\chi_{\mathrm{H}}}{kT}\right)^{1/2} \times F_0 \int_0^\infty \left(\frac{kT}{h\nu}\right)^{1/2} e^{-(\nu-\nu_0)^2/(\Delta\nu)^2} e^{-h\nu/kT} \mathrm{d}\nu. \tag{15}$$

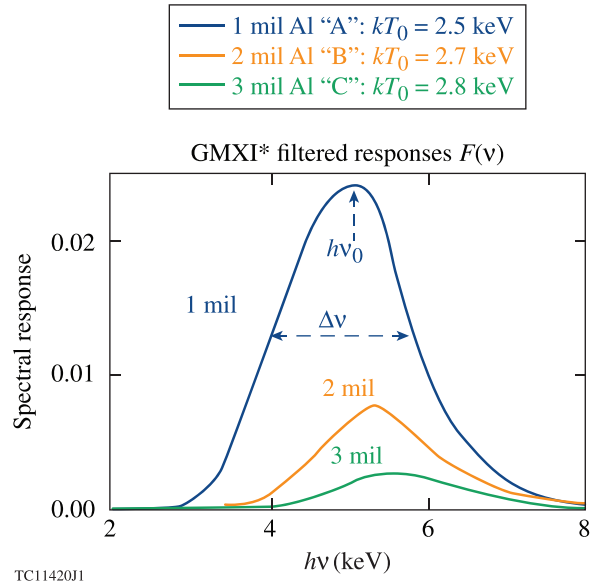


FIG. 2. Plot of the GMXI[29] camera spectral-response functions for three of its channels. These channels differ by the thicknesses of the Al filter layers in their respective filter packages. The emissivity of a source, integrated over one of these response functions, will be exclusively dependent on the pressure of the source when the source temperatures fall within a narrow range near the ideal source temperature $kT_0$ indicated for that channel.

For the anticipated small values of the parameters $\Delta\nu/\nu_0$ and $h\Delta\nu/kT$, we use the leading-order approximation

$$\left(\frac{h}{kT}\right)^{1/2} \int_0^\infty e^{-(\nu-\nu_0)^2/(\Delta\nu)^2} e^{-h\nu/kT} \frac{\mathrm{d}\nu}{\nu^{1/2}} \simeq \sqrt{\pi} \frac{\Delta\nu}{\nu_0} \left(\frac{h\nu_0}{kT}\right)^{1/2} e^{-h\nu_0/kT}, \tag{16}$$

and we write

$$E_{\nu_0,\Delta\nu} = \frac{16}{3} \alpha^3 \chi_{\mathrm{H}} a_0^3 \beta F_0 \Delta\nu \left(\frac{P}{kT}\right)^2 \left(\frac{\chi_{\mathrm{H}}}{h\nu_0}\right)^{1/2} e^{-h\nu_0/kT}. \tag{17}$$

Near any given temperature, the temperature dependence of Eq. (17) can be treated as a power law $y \sim x^\eta$ fit to the actual temperature dependence of the form

$$y = \frac{e^{-1/x}}{x^n}, \tag{18}$$

where $x = kT/h\nu_0$. The exponent $\eta$ near a particular value of $x$ is

$$\eta = \frac{x}{y}\frac{\mathrm{d}y}{\mathrm{d}x} = \frac{1 - nx}{x}. \tag{19}$$

Solving for $\eta = 0$ gives $x = 1/n$. The temperature dependence of Eq. (17) is the $n = 2$ case, which gives

$$kT_0 = \frac{h\nu_0}{2} \tag{20}$$

as the condition for stationary maximum integrated emissivity with respect to temperature. So while Eq. (17) is

explicitly temperature dependent, it can be regarded as independent of temperature within a limited range of temperature centered at $kT_0$. If the KL fit given above were used rather than the asymptotic Kulsrud expression, Eq. (18) would be replaced by $y = e^{-1/x}/x^{2.09}$, displacing the stationary point of the emissivity to $kT_0 = h\nu_0/2.09$, which is almost the same as Eq. (20) for the purposes of this discussion. The applicable range of temperature is easy to determine directly from Eq. (17) for a desired tolerance. For example, the integrated emissivity will be within 90% of its maximum (representing a ±5% minimum-to-maximum variation) at $kT_0 = 2.65$ keV over the temperature range $1.95\,\text{keV} < kT < 3.73\,\text{keV}$ for the GMXI "B" response function with the $h\nu_0 = 5.30$-keV center energy. This temperature range is representative of cryogenic ICF implosion hot spots.

What we now have in Eq. (17) is an expression for emissivity that is a function of pressure alone, as long as the spectral response of the detector is appropriately matched to the source temperature range. A nominal temperature value or profile must be provided to evaluate Eq. (17), but if the source–instrument matching condition given by Eq. (20) is satisfied closely enough, the emissivity can be treated as a function of pressure alone. If the source temperature profile does deviate from satisfying Eq. (20) to a degree that the emissivity temperature dependence at fixed pressure cannot be ignored, Eq. (17) is still valid, but temperature profile input must then resemble the actual temperature profile closely enough to avoid throwing off the relationship between the emissivity and the pressure profiles. A temperature profile from a simulation may suffice.

## III. INFERRING HOT-SPOT PRESSURE FROM X-RAY EMISSION MEASUREMENTS

The expression for Abel inversion given by Eq. (4) and the emissivity expression in terms of pressure given by Eq. (17) allow the pressure profile to be inferred from the imaged specific intensity $I_{\nu_0}(x)$. This will be demonstrated using a simulated image of OMEGA cryogenic implosion shot 68 791 (Ref. 30). The implosion is simulated with the one-dimensional (1-D) radiation–hydrodynamics code *LILAC*,[31] and the images are calculated using the post-processor *Spect3D*.[32] The temperature, density, and pressure profiles of this implosion at 1.94 ns—the time of stagnation and peak neutron production—are shown in Fig. 3. A GMXI image of the emission from this configuration simulated with *Spect3D*, using the spectral response function "B" with 2-mil Al filtering shown in Fig. 2, is shown as the solid dark gray (orange online) curve in Fig. 4. *Spect3D* uses the actual response functions specified for the GMXI [not the Gaussian approximation used in deriving Eq. (17)] and Gaunt factors based on the KL model extended to include the effects of electron degeneracy.[23] *Spect3D* calculates a full solution of the equivalent of Eq. (1), taking into account all emission and absorption effects within the entire imploded configuration.

The simulated imploded configuration in Fig. 3 is substantially isobaric at $P \approx 22$ Gbar out to the radius indicated by the vertical dashed line at 34 $\mu$m. In the simulated

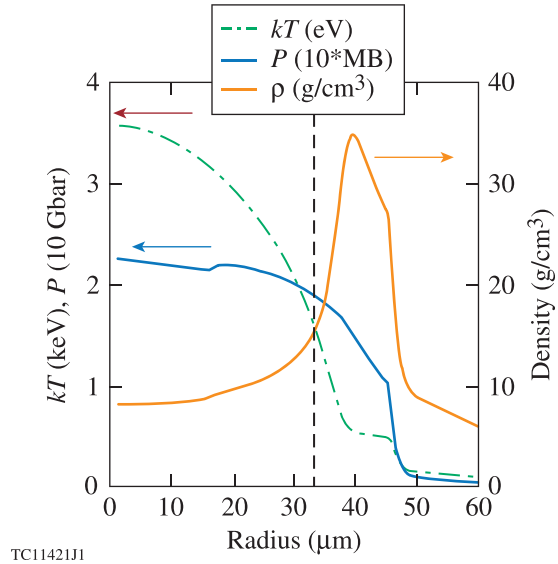


FIG. 3. Simulated OMEGA cryo shot 68 791 (Ref. 30) profiles at 1.94 ns, the time of peak neutron production. The hot spot ($kT > 1.5$ keV) appears to be substantially isobaric at $P \approx 22$ Gbar out to the radius indicated by the vertical dashed line at 34 $\mu$m. In the simulated instantaneous image at this time, this distance represents the radius of the 17% intensity contour,[33] which is also shown for reference on the image plots in Figs. 4–6.

instantaneous image at this time shown in Fig. 4 and in the plot of the simulated time-integrated image in Fig. 5, this distance represents the radius of the 17% intensity contour of the instantaneous image, which has been suggested as one criterion to use in measuring the size of a hot spot from its

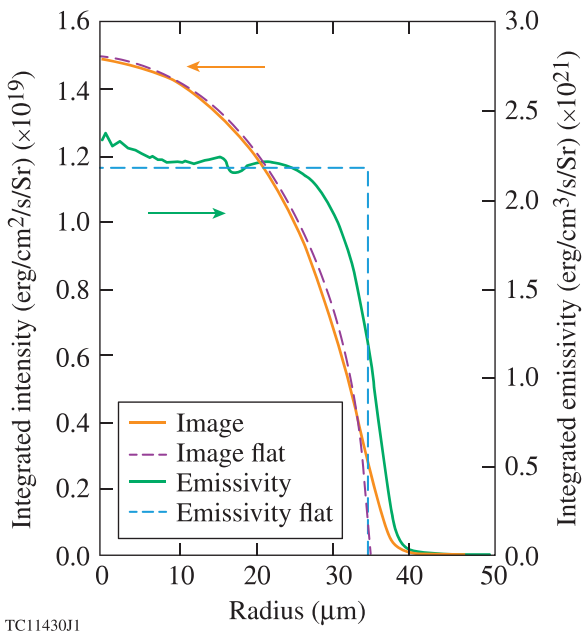


FIG. 4. The filtered simulated GMXI image of the simulated implosion core of OMEGA shot 68 791 at 1.94 ns—the time of peak neutron production. The left axis is the "B"-channel integrated intensity distribution of the simulated image [solid dark gray (orange) curve (Image)]. The right axis is the emissivity profile obtained from the inverse Abel transform of the simulated image [solid light gray (green) curve (Emissivity)]. The image is almost indistinguishable from the dashed dark gray (purple) curve (Image flat) (left axis), which is the image of a perfectly flat emissivity profile represented by the dashed light gray (blue) curve (Emissivity flat) (right axis) extending out to $r = 34\,\mu$m.

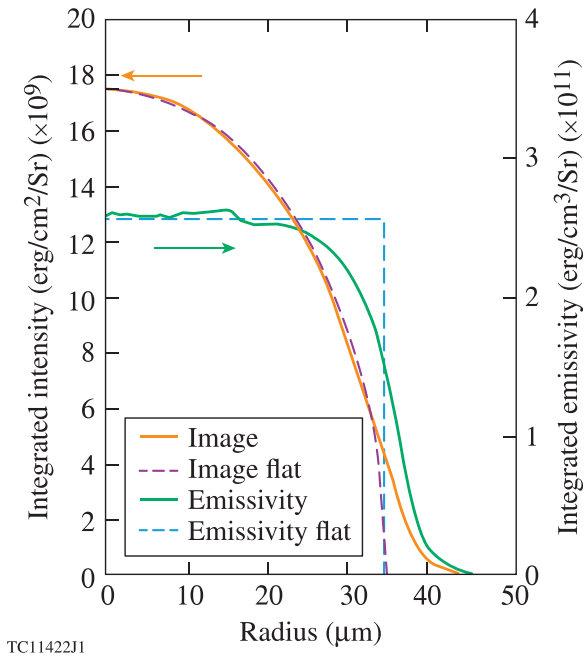


FIG. 5. The filtered simulated GMXI image of the simulated implosion core of OMEGA shot 68 791 integrated over a 300-ps time window centered at 1.96 ns. This interval includes the times of stagnation, peak neutron production, and peak x-ray intensity. All plotted quantities in this figure are time integrated. The left axis is the intensity distribution of the simulated image [solid gray (orange) curve (Image)]. The right axis is the emissivity profile obtained from the inverse Abel transform of the image [solid light gray (green) curve (Emissivity)]. Out to near $r = 34\,\mu$m, the image is almost indistinguishable from the dashed dark gray (purple) curve (Image flat) (left axis), which is the image of a perfectly flat emissivity profile represented by the dashed light gray (blue) curve (Emissivity flat) on the right axis.

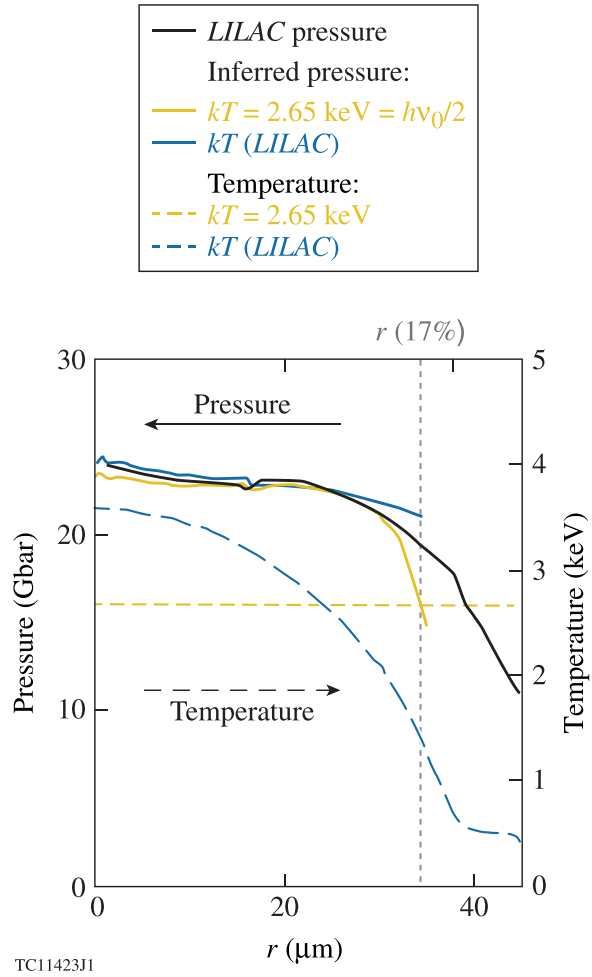


FIG. 6. Pressure profiles inferred from the simulated GMXI image shown in Fig. 4 of the simulated implosion core of OMEGA shot 68 791 at 1.94 ns—the time of peak neutron production. The pressure profiles were obtained using Eq. (17) from the emissivity profile obtained from the simulated image by Abel inversion. From the left axis, the pressure profile plotted as the lower solid lighter gray (yellow) curve was obtained assuming the ideal $kT_0 = 2.65$ keV nominal temperature based on the GMXI response centered at 5.30 keV, represented on the right axis by the dashed gray (yellow) curve, and the pressure profile plotted from the left axis as the upper dark gray (blue) curve was obtained by assuming the radius-dependent temperature profile from the *LILAC* hydrodynamic simulation on the right axis represented by the dashed lighter gray (blue) curve. The vertical dashed line indicates the 17% intensity contour radius—the nominal outer radius of the hot spot.

image.[33] This criterion appears to coincide with other criteria that are more physically significant, although not as directly measurable, such as the inner half-peak density point of the imploding mass distribution in Fig. 3 or the half-emissivity radius seen in Figs. 4 and 5. The temperature range within this so-defined hot spot is roughly $1.5\,\text{keV} < kT < 3.5\,\text{keV}$, which extends only slightly below the temperature range given in Sec. II for a $\pm 5\%$ accuracy limit on Eq. (17) with a nominal temperature of $kT_0 = 2.65$ keV. Therefore, the flat pressure profile in Fig. 3 results in the similarly flat emissivity profile seen in Fig. 4, even as the temperature varies. This insensitivity of the inferred pressure profile to the assumed temperature profile over the radial range of the hot-spot profile is seen more clearly in Fig. 6.

The solid dark gray (orange online) curve in Fig. 4 is the simulated instantaneous radial intensity distribution of the image, obtained using the "B" response function, of the OMEGA cryogenic implosion shot 68 791 at 1.94 ns—the time of stagnation and peak neutron production shown in Fig. 3. The solid light gray (green online) curve is the emissivity profile obtained from the inverse Abel transform of this image using Eq. (4). The image is almost indistinguishable from the dashed dark gray (purple online) quarter-ellipse, which is exactly what Eq. (5) predicts for the image of a flat emissivity profile extending out to $R = 34\,\mu$m, shown in Fig. 4 as the dashed light gray (blue online) profile. The relative deviations of the simulated image from the elliptical image are very small, in contrast with the larger relative deviations of the simulated emissivity from a flat emissivity profile. This is understood as the smoothing effect of the integration in Eq. (2) on the emissivity profile.

Figure 5 is virtually identical to Fig. 4 in every respect, other than a relative factor of about 110 ps, which can be taken as the emission time scale. This simulated image intensity has been integrated over a 300-ps time window centered at 1.96 ns, long enough to include both the x-ray and neutron emission times. Again, as was the case with the results shown in Fig. 4, the image deviates very little from the elliptical shape, while the simulated emissivity profile deviates more visibly from a flat profile near the outer radius of the hot spot.

The pressure profile of an imploded hot spot can be inferred using Eq. (17) from the emissivity profile obtained

by Abel inversion of the simulated image using Eq. (4). As discussed in Sec. II, this inferred pressure is insensitive to the assumed temperature profile if the camera response is centered at $h\nu_0 = 2kT_0$, where the hot-spot temperatures are within a limited range of $T_0$. Exactly how closely the emissivity profile follows the pressure profile will depend on how far the range of the hot-spot temperature deviates from $T_0$, as has been described in Sec. II. In principle, any nominal $T$ value or radial $T(r)$ profile can be used with Eq. (17). For example, this nominal temperature can be the ideal temperature $T_0$ matched to the instrument response, or it can be the logarithmic slope of the hard end of the continuum spectrum, if it has been measured. Ignoring the Gaunt factor in Eq. (8) leaves one with the simple $\varepsilon_\nu^{\mathrm{FF}} \sim e^{-h\nu/kT}$ frequency dependence. The additional factor $(kT/h\nu)^{1/2}$ in Eq. (12) bends the logarithmic slope slightly

$$-\frac{\mathrm{d}\ln\left(\varepsilon_\nu^{\mathrm{FF}}\right)}{\mathrm{d}h\nu} = \frac{1}{kT_{\mathrm{inferred}}} = \frac{1}{kT} + \frac{1}{2h\nu}, \tag{21}$$

but the fractional error in the temperature inferred from measuring the spectral logarithmic slope $\delta T/T \approx kT/2\,h\nu$, can be minimized by measuring as high in spectral energy as possible. Using Eq. (17) with a radially dependent simulated temperature profile could provide more-accurate results than a constant nominal temperature.

Using Eq. (17) to infer a pressure profile from an emissivity profile is demonstrated in Fig. 6 for the case of shot 68 791 shown in Fig. 4. Pressure profiles inferred from the simulated GMXI "B"-channel image of the simulated implosion core of OMEGA shot 68 791 shown in Fig. 4 at 1.94 ns—the time of peak neutron production. The pressure profiles were obtained using Eq. (17) from the emissivity profile obtained from the simulated image by Abel inversion. The pressure profile plotted as the solid light gray (orange online) curve was obtained assuming the ideal $kT_0 = 2.65$ keV nominal temperature based on the GMXI response centered at 5.30 keV, represented as the dashed light gray (orange online) line, and the pressure profile plotted as the dark gray (blue online) curve was obtained by assuming the radius-dependent temperature profile from the *LILAC* hydrodynamic simulation plotted as the dashed dark gray (blue online) curve. The vertical dashed line indicates the 17% intensity (half-emissivity) contour radius—the nominal outer radius of the hot spot. Even with these two very different assumed temperature profiles, the two inferred pressure profiles agree with the simulated pressure profile very well, up to within a short distance of the edge of the hot spot.

## IV. SCALING RELATIONSHIPS OF THE X-RAY YIELD OF AN ISOBARIC HOT SPOT AT STAGNATION

The energy-integrated emissivity of an isobaric hot spot tracks its flat pressure profile nearly all the way to its outer radius $R$, provided that the source temperature profile does not deviate too far from the $T_0$ set by the condition $h\nu_0 = 2kT_0$, where $h\nu_0$ is the center of the instrument response function. If the emissivity per volume is reasonably uniform over the entire hot spot, as is the case in the example shown in Fig. 4, the hot spot will produce a total filtered radiated energy or photon yield of

$$Y_{\nu_0} = 4\pi\left(\frac{4\pi}{3}R^3\right)\Delta t E_{\nu_0}, \tag{22}$$

where the leading factor of $4\pi$ represents integration of the isotropic emissivity over the full sphere of solid angle. If the gate time or exposure time $\Delta t$ exceeds the lifetime of the hot spot, the total effective emission time $\Delta t$ must be inferred from another measurement, such as the neutron yield $Y_{\mathrm{n}}$, assuming that both the neutron and photon emission are limited by the same hot-spot lifetime. With a radius $R$ obtained from the GMXI image and the temperature dependence relatively weak, a useful estimate of the hot-spot pressure can be obtained from Eqs. (17) and (22). This was done for a sizable ensemble of cryogenic implosion simulation results.[30] The inferred pressures are compared in Fig. 7 with the simulated central peak pressures. The simulated photon yield was the time-integrated B-channel emission, the emission time in Eq. (22) is the quotient of the simulated neutron yield divided by the peak neutron-production rate, and the image size is the 17%-intensity contour of the simulated GMXI image. The ensemble of implosions includes shell adiabat parameters over the range $1.5 < \alpha_{\mathrm{shell}} < 3.5$ and neutron yields over the range $1.3 \times 10^{13} < Y_{\mathrm{n}} < 1.3 \times 10^{14}$. The close agreement between the pressures inferred from the simulated images and the simulated pressure values is convincing, although not entirely expected, in light of the combined systematic inaccuracy that might result from equating the photon and neutron emission lifetimes, using the reasonable but not unique choice of the 17% contour as the hot-spot radius, and from assuming that the emissivity of the entire hot spot is determined by the central pressure at stagnation alone. This effectively confirms that the agreement between

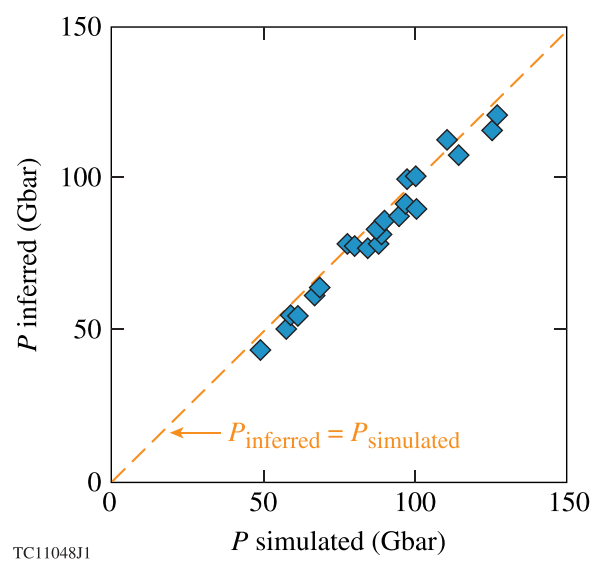


FIG. 7. The hot-spot pressure inferred from *LILAC*/*Spect3D* simulated images shown in very good agreement with the simulated peak central pressure. Equations (17) and (22) give accurate hot-spot pressures from simulated images for an ensemble of cryogenic simulations representing a broad range of shell adiabat parameters and neutron yields.

the simulated and inferred central pressures in Fig. 6 is obtained for every implosion in this ensemble.

A few interesting new expressions for the scaling of the photon yield with various parameters of the implosion can be obtained from Eqs. (17) and (22). First, we write

$$M_{\mathrm{Sh}}\frac{R}{(\Delta t)^2} = 4\pi R^2 P, \tag{23}$$

saying that the imploding thin unabated shocked shell of mass $M_{\mathrm{Sh}}$ surrounding the hot spot of radius $R$ experiences an outward acceleration $R/(\Delta t)^2$ at stagnation, where $\Delta t$ is the scale time of the bounce of shell, by the force of the hot-spot pressure $P$ acting on the inner surface of the shell.[12]

Next, we can write the adiabatic scaling of the hot-spot pressure with respect to the hot-spot volume $V = 4\pi R^3/3$ as

$$P \propto \alpha_{\mathrm{HS}} V^{-5/3}, \tag{24}$$

where $\alpha_{\mathrm{HS}}$, a hot-spot "adiabat" parameter, distinguishes among the hot spots of different implosions. The stagnating hot-spot material is not adiabatic in the usual sense, where the pressure would scale with the hot-spot density as $P \propto \alpha_{\mathrm{HS}}\rho^{-5/3}$, because of heat flow out of and material flow into the hot spot. The hot-spot volume, however, can be treated as an adiabatic enclosure because the heat conduction out of the hot spot is exactly compensated by the heat of the material ablated off the inner surface of the shell back into the hot spot at the hot-spot boundary.[12] Together, Eqs. (23) and (24) give the volume–time product

$$V\Delta t \propto \frac{(\alpha_{\mathrm{HS}} M_{\mathrm{Sh}})^{1/2}}{P} \tag{25}$$

needed in Eq. (22). Applying Eq. (17), subject to the conditions given in Sec. II for temperature-independent emissivity, we obtain the expression

$$Y_{\nu_0} \propto (\alpha_{\mathrm{HS}} M_{\mathrm{Sh}})^{1/2} P, \tag{26}$$

which predicts that the photon yield will scale in direct proportion to the hot-spot pressure for an ensemble of similar cryogenic implosions. This linear scaling is verified in Fig. 8 for the same set of simulations used to obtain the results shown in Fig. 7, although with more scatter. This additional scatter may reflect the simplification of the hot-spot dynamics by Eq. (23) and the simplification of the hot-spot energy balance by Eq. (24) or by the variations in the product $\alpha_{\mathrm{HS}} M_{\mathrm{Sh}}$ over the ensemble. Accounting for all the details of Fig. 8 is beyond the scope of this paper, but for now, Fig. 8 suffices to add validity to the scaling arguments that have been made.

The sample of 1-D OMEGA cryogenic implosion simulations illustrated in Figs. 7 and 8 displays a curious scaling of the simulated photon yield with the neutron yield, $Y_{\nu_0} \propto Y_n^{0.57}$, shown in Fig. 9 (Ref. 30). The value of the scaling index, as well as the fact that the photon and neutron yields appear to fall along a single curve, can be explained in terms of the dynamics of isobaric implosion cores at stagnation. We begin again with the photon yield given by

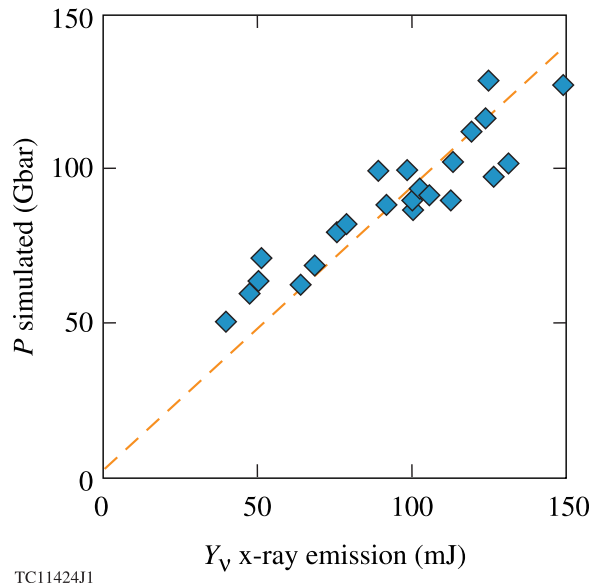


FIG. 8. The hot-spot pressure simulated by *LILAC* shown following the predicted linear scaling with the photon yield. The hot-spot pressure is predicted to vary in direct proportion to the x-ray yield for an ensemble of similar cryogenic implosions with shell adiabat parameters and neutron yields that vary over a wide range.

Eqs. (17) and (22), this time keeping track of the precise temperature scaling of the photon- and neutron-production rates. We allow that the scaling index $\eta$ of the temperature dependence of Eqs. (18) and (19), as in

$$y = \frac{e^{-1/x}}{x^2} \propto x^{\eta}, \tag{27}$$

may deviate from $\eta = 0$. We expect that $\eta$ will be small since our instrumentation and emission source place us near $h\nu_0 = 2kT_0$, but the scaling calculation below does not require this. We apply Eqs. (17), (22), and (27) and obtain

$$Y_{\nu_0} \propto P^2 T^{\eta} V \Delta t. \tag{28}$$

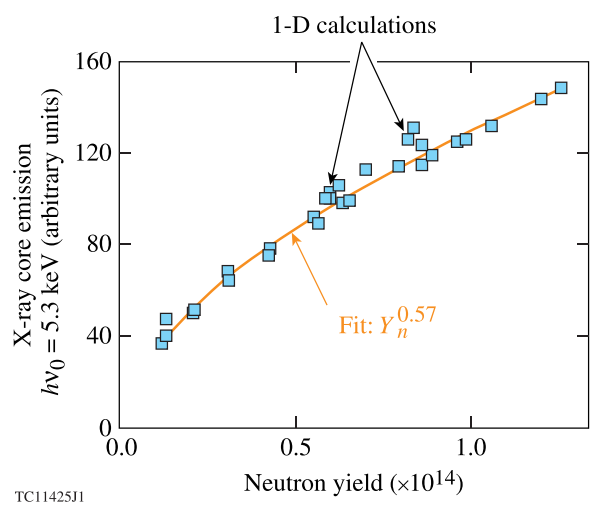


FIG. 9. Photon-neutron yield scaling in cryo implosion simulations.[30] The x-ray yields of an ensemble of cryo implosion simulations have been found to scale with the 0.57 power of their respective neutron yields over a broad range of shell adiabats and neutron yields.

The neutron yield can be written using the deuterium–tritium (DT) reaction rate

$$\langle \sigma v \rangle \propto T^{4+\varepsilon}, \tag{29}$$

where we obtain the small deviations $|\varepsilon| \ll 1$ from a fixed temperature scaling using the reaction rate by Bosch and Hale.[34] The neutron yield is written as the volume and time integral

$$Y_{\mathrm{n}} = \int\int n_{\mathrm{D}} n_{\mathrm{T}} \langle \sigma v \rangle \mathrm{d}V \mathrm{d}t \propto P^2 T^{2+\varepsilon} V \Delta t. \tag{30}$$

The neutron-production rate is a function of the deuterium–-tritium density product $n_D n_T$ and the ion temperature, so combining Eq. (29) with the ideal gas equation of state to form Eq. (30) is another application of the $T_e = T_i$ equilibrium assumption made earlier. While the x-ray emissivity can be approximated fairly well as uniform over the volume of an isobaric hot spot, the neutron production varies as an additional two powers of temperature and, as a result, will be more center peaked and possibly shorter in duration. Nevertheless, we proceed assuming that the usual approximation—that the source volumes and emission times of the neutrons and photons are the same—is valid to within constant factors that drop out of scaling relationships, and we apply Eqs. (24), (25), (28), and (30) to obtain

$$Y_{\nu_0} \propto \left( \frac{M_{\mathrm{Sh}}^{2/9} M_{\mathrm{HS}}^{10/9}}{\alpha_{\mathrm{HS}}^{4/9}} \right)^p Y_{\mathrm{n}}^q, \tag{31}$$

where

$$p = \frac{1 + (\varepsilon - \eta)/2}{1 + 2\varepsilon/9} \tag{32}$$

and

$$q = \frac{5 + 2\eta}{9 + 2\varepsilon}. \tag{33}$$

For the nominal values $\eta = \varepsilon = 0$, this gives $q = 0.56$ for the neutron-yield scaling exponent, which is very close to the value obtained from the simulation ensemble, as shown in Fig. 9. In Eq. (31), the three constant stagnation parameters $\alpha_{\mathrm{HS}}$, $M_{\mathrm{Sh}}$, and the hot-spot mass $M_{\mathrm{HS}} \sim R^3 P/T$ combine in a product where the scaling relative to each other is fixed. We have chosen to write Eq. (31) with this three-parameter product scaled such that $p = 1$ for the nominal values $\eta = \varepsilon = 0$. The effects of variations of $\alpha_{\mathrm{HS}}$, $M_{\mathrm{Sh}}$, and $M_{\mathrm{HS}}$ throughout the simulation ensemble and the effects of the temperature-dependent scaling corrections $\eta$ and $\varepsilon$ will be considered below, but for now the successful derivation of the value of the scaling exponent $q$ is clearly an encouraging validation of the scaling calculations so far.

The alignment of the simulated data points in Fig. 9 along a single curve does make sense in light of Eq. (31). The neutron yield varies over the ensemble by an order of magnitude, and the scatter about the curve, attributable to variations in $\alpha_{\mathrm{HS}}$, $M_{\mathrm{Sh}}$, and $M_{\mathrm{HS}}$, is relatively small. Extracting precise values of these three parameters from simulations depends on the time resolution of the simulation output as well as on somewhat arbitrary definitions, but it is clear that the net effect of their variations is much less than the ranges of the neutron and photon yields. It is interesting to note that the temperature-dependent scaling corrections pertain only to the microphysics of photon and neutron production, not the design or dynamics of the implosion capsules. Were this yield–yield plot generated with simulations or measurements of a different ensemble of isobaric implosions with target masses scaled up by significant factor, for example, Eqs. (31)–(33) predict that the overall proportionality constant would change with the mass and hot-spot adiabat parameter, but the yield-scaling exponent would be the same for the same spectral response and source temperatures.

The result $q = 0.56$ quoted above is obtained only with the nominal values $\eta = \varepsilon = 0$. Taking this temperature dependence into account, $q$ is found to be a relatively insensitive function of temperature. For example, the range $q = 0.57 \pm 0.06$ is obtained, in reasonably good 10% agreement with the value $q = 0.57$ in Fig. 9, for the relatively broad range of temperature $kT = 2.21 \pm 0.43$ keV. Even though the yield scaling exponent is relatively insensitive to variations in the hot-spot temperature, it may have diagnostic value through its temperature dependence. If the fit to KL results for the FF Gaunt factor described above were used in place of Eq. (11), the effect would be to reduce $\eta$ by 0.09, which would reduce the predicted $q$ values by 3.6% overall.

Equation (31) accounts for the yield-scaling behavior shown in Fig. 9 because the scaling index given by Eq. (32) agrees with the fit to the simulation ensemble for typical hot-spot temperatures and because the scaled product $M_{\mathrm{Sh}}^{2/9} M_{\mathrm{HS}}^{10/9} \alpha_{\mathrm{HS}}^{-4/9}$ of stagnation parameters has negligible correlations with both the photon and neutron yields. The simulation ensemble was constructed to follow a long series of cryogenic implosion experiments as closely as possible; the experiments were not designed to control this product. If this product did have a significant correlation with either the photon or neutron yields, then Eq. (32) would not agree with the yield scaling exhibited by the simulation ensemble.

A slightly modified version of Eq. (31) can be derived by using the scaling expression

$$M_{\mathrm{HS}} \sim M_{\mathrm{Sh}}^{1/7} P^{4/7} R^{16/7} \tag{34}$$

for the hot-spot mass given by Zhou and Betti.[35] We use this to remove $M_{\mathrm{HS}}$ from the calculation, giving the result

$$Y_{\nu_0} \propto (M_{\mathrm{Sh}}^{4/11})^{p'} Y_{\mathrm{n}}^{q'}, \tag{35}$$

where

$$p' = \frac{1 + (\varepsilon - \eta)/2}{1 + 2\varepsilon/11} \tag{36}$$

and

$$q' = \frac{7 + 2\eta}{11 + 2\varepsilon}. \tag{37}$$

These are only a slight departure from Eqs. (31)–(33). Remarkably, the only stagnation parameter appearing is $M_{\rm Sh}$, or, in other words, the normalized photon yield $Y_{\nu_0}/Y_{\rm n}^{q'} \sim M_{\rm Sh}^{4p'/11}$ is a function of the shell mass alone.

The two sets of equations [Eqs. (31)–(33) and Eqs. (35)–(37)] are both correct, but the latter is the more-final result, with some hot-spot parameter dependences eliminated. This was accomplished by introducing Eq. (34), which brings additional approximations into the calculation that were made to evaluate thermal transport in evolving inner-shell density and temperature profiles.[12] These are the same approximations that were made in establishing the hot-spot adiabatic behavior expressed as Eq. (24); the hot-spot pressure varies adiabatically with respect to the hot-spot volume during the approach to stagnation.

The $p'$ and $q'$ values obtained from Eqs. (36) and (37), respectively, are plotted as functions of hot-spot temperature in Fig. 10 as solid gray (orange online), right-hand scale, and solid black, left-hand scale, curves, respectively. The left-hand scale is only one-fifth the numerical length of the right-hand scale, indicating that $q'$, like $q$, is a relatively insensitive function of temperature. The respective temperature-scaling indices $\varepsilon$ and $\eta$ of the photon- and neutron-production rates are also plotted in this figure. The gray (blue online) shaded range of temperature corresponds to the temperature range of $kT = 2.5$ to 3.1 keV, which is the one-standard-deviation range of the neutron-averaged temperature values of the simulations in the ensemble represented in Fig. 9. The $q'$ curve reflects this temperature range onto the corresponding shaded range of $q'$ values. This range of $q'$ values includes the value $q' = 0.57$ value obtained from the simulation ensemble in Fig. 9. This shows that Eq. (37) is consistent with the yield scaling index obtained from the simulation ensemble in Fig. 9 for typical hot-spot temperatures. Equation (35) is likewise consistent with the same value, $q = 0.57$, but at slightly lower temperatures that are also typical of hot-spot stagnation conditions. With Eq. (37), however, consistency is obtained with neutron-averaged temperatures, which are characteristic of the neutron source, making this perhaps the more-convincing demonstration of consistency.

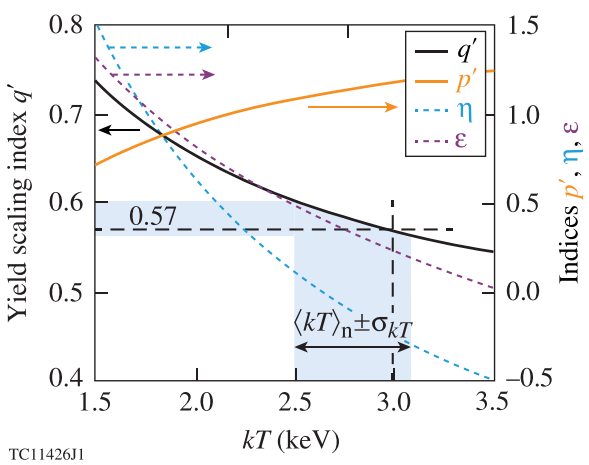


FIG. 10. Yield-scaling indices $p'$ and $q'$ and the photon and neutron temperature-scaling indices $\eta$ and $\varepsilon$ plotted as functions of temperature. The yield-scaling indices $p'$ [plotted as the solid gray (orange) curve from the right axis] and $q'$ (solid black curve from the left axis) are functions of temperature through the temperature-dependent scaling indices $\eta$ [dashed light gray (blue) curve from the right axis] and $\varepsilon$ [dashed dark gray (purple) curve from the right axis] of the photon- and neutron-production rates, respectively. The $q'$ curve shows that the $q' = 0.57$ value from Fig. 9 is within the range of $q'$ corresponding to the temperature range $kT = 2.5$ to 3.1 keV, which is within one standard deviation of the mean neutron-averaged temperature of the simulation ensemble shown in Figs. 7 and 8. These ranges of $q'$ and $kT$ are shown highlighted with gray (blue) shading and are seen to be related by $q'$ versus $kT$ (black curve).

## V. ENHANCED X-RAY EMISSION AS A MEASURE OF FUEL–SHELL MIX

The yield scaling results in Fig. 9 were obtained from *LILAC*[31] 1-D hydrodynamic simulations, which do not model unstable hydrodynamic behavior. Implosions with shell adiabat parameters in the lower end of the range $1.5 < \alpha_{\rm shell} < 3.5$ have thinner shells that are more susceptible to the Rayleigh–Taylor instability[36] during the deceleration phase of the implosion. Breakup of the unstable shell would leave some amount of the shell carbon mixed into the hot spot at the time of stagnation. Since carbon is much more emissive than hydrogen, very small concentrations of carbon can significantly increase the x-ray emission. Since the simulated photon and neutron yields in Fig. 9 exhibit a $Y_{\nu_0} \propto Y_{\rm n}^{0.57}$ behavior, the normalized simulated yield quotient $Y_{\nu_0}/Y_{\rm n}^{0.57}$ forms a constant normalized photon yield when plotted as a function of any quantity, such as the shell adiabat parameter, as shown by the blue squares in Fig. 11. The same quantity derived from actual measured yields is plotted as orange circles. These values are generally constant, in agreement with the 1-D simulated results, for shell adiabat parameter values above the $\alpha_{\rm shell} \approx 2.3$ value, but they show a distinct excess photon yield below this point. This has been

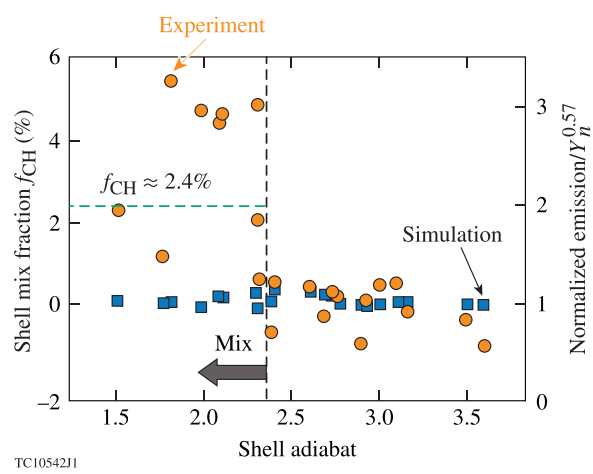


FIG. 11. Excess photon yield as a measure of fuel–shell mix. The normalized yield quotient $Y_{\nu_0}/Y_{\rm n}^{0.57}$ is nearly constant for the simulated implosions, according to the results plotted here and in Fig. 9 as (blue) squares. The same quotient calculated from measured yields is plotted as (orange) circles. These measurements conform to the 0.57 power scaling for higher shell adiabat parameters $\alpha_{\rm shell} > 2.3$. As unstable shells break up during the deceleration phase of the implosion, carbon can be mixed into the hot spot from the shell, which accounts for the excess x-ray emission above the amount expected from the yield scaling. This twofold to threefold enhancement can be attributed to masses of 125 to 250 ng of shell CH mixed uniformly into the hot spot. (Figure 8 from Ref. 30).

attributed to the expected contamination of the hot spot by shell carbon. We extend this analysis to infer the mass of shell material mixed into the hot spot from measurements of this excess emission.

Using the FF emission of hydrogen as a pressure diagnostic assumes a pure hydrogen core. Any mix of non-hydrogen into the hot spot will raise the per-ion emissivity of the hot spot. The twofold-to-threefold enhancement of the normalized measured hot-spot emission shown in Fig. 11 for low-adiabat implosions can be interpreted in terms of contamination of the hot spot by shell carbon. The emission from a carbon-contaminated hot spot will have a strong contribution from radiative recombination, which is FB emission, the time inverse of photoionization or bound-free (BF) absorption. The carbon emission will have comparable FF and FB contributions with much stronger total emission per ion than hydrogen.

Following a conventional approach, we discuss the combined FF and FB emissivity in parallel by considering their respective absorption cross sections. The Kramers photon absorption cross sections are

$$\sigma_{\rm FF}(\nu) = \frac{256\pi^{5/2}}{3\sqrt{3}}\alpha a_0^5 n_{\rm e} Z^2 \left(\frac{\chi_{\rm H}}{kT}\right)^{1/2}\left(\frac{\chi_{\rm H}}{h\nu}\right)^3 g_{\rm FF} \tag{38}$$

for FF absorption by an ion of total charge $Z$ and

$$\sigma_{\rm BF}(\nu) = \begin{cases} \dfrac{64\pi}{3\sqrt{3}}\alpha a_0^2 \dfrac{Z^4}{p^5}\left(\dfrac{\chi_{\rm H}}{h\nu}\right)^3 g_{\rm BF}; & h\nu \geq \chi_p \\ 0; & h\nu < \chi_p \end{cases} \tag{39}$$

for BF absorption by the photoionization of the single electron bound to a nucleus of charge $Z$ in principal quantum level $p$ (Ref. 10). We keep the explicit dependence of $\sigma_{\rm BF}(\nu)$ on $p$ for now, but only the ground-state $p = 1$ photoionization contribution will be significant. The Gaunt factors $g_{\rm FF}$ and $g_{\rm BF}$ account for departures from the Kramers semi-classical approximation. Based on the micro-reversibility of each process, the Gaunt factor for emission also applies to absorption. The ionization-edge cutoff energy $\chi_p$ of the BF cross section is the ionization energy of the bound electron in the $p$ shell. This can be expressed using the Bohr formula $\chi_p = Z^2\chi_{\rm H}/p^2 - \Delta\chi$. We only mention continuum lowering[37] $\Delta\chi$ for completeness, showing only its effect on $\chi$. Since x-ray measurements are made far above this $h\nu = \chi_p$ cutoff, we will not consider it further. Further discussion beyond the scope of this paper should consider continuum lowering and other high-density effects in more detail.

The hot-spot plasma is accurately described as nearly completely ionized, with the fully ionized atoms accounting for essentially all the FF and FB emission and with only a trace of the H-like species remaining to provide BF absorption. We neglect excited states and consider only the density $n_{i,1}$ of ground-state ($p = 1$) H-like ions and the density $n_{i,2}$ of the fully stripped species, so that $n_{i,1} + n_{i,2} = n_i$, where $n_i$ is the total ion density of element $i$. Certainly for hydrogen and carbon, $n_{i,1}$ will be very small, and all other ionization species can be neglected. Using criteria provided in Ref. 10, it is easily verified that hot-spot stagnation times are far longer and densities are far higher than those required to maintain collision-dominated, detailed-balance, quasi-static local thermodynamic equilibrium (LTE) ionization-species populations. Therefore, we may use the Saha equation[10]

$$\frac{n_{i,2}n_e}{n_{i,1}} = \frac{2}{a_0^3}\frac{g_2}{g_1}\left(\frac{kT}{4\pi\chi_{\rm H}}\right)^{3/2} e^{-\chi_i/kT}, \tag{40}$$

where $g_1$ and $g_2$ are the statistical weights of the bound and stripped states, respectively. The statistical weights for H-like and stripped ions are $g_1 = 2p^2$ and $g_2 = 1$, respectively.

The FF opacity $\kappa_\nu^{\rm FF}$ for the fully ionized species with nuclear charge $Z$,

$$\kappa_\nu^{\rm FF} = \frac{256\pi^{5/2}}{3\sqrt{3}}\alpha a_0^5 n_{\rm e} n_{i,2} Z^2 g_{i,\rm FF}\left(\frac{\chi_{\rm H}}{kT}\right)^{1/2}\left(\frac{\chi_{\rm H}}{h\nu}\right)^3 (1 - e^{-h\nu/kT}), \tag{41}$$

accounts for the entire FF contribution from that element since lower degrees of ion ionization contribute less, in proportion to their fractional populations. We can be more precise now by stipulating that the Gaunt factor $g_{i,\rm FF}$ pertains to the fully stripped species of element $i$. The correction for stimulated emission is included. Considering a mixture of elements $i$, using $n_2 \approx n_i$, we have $\sum_i n_i Z_i^2 g_{\rm i,Z,FF} = n_{\rm i}\langle Z^2 g_{\rm Z,FF}\rangle$, where $n_{\rm i}$ is the total ion density, and

$$\kappa_\nu^{\rm FF} = \frac{256\pi^{5/2}}{3\sqrt{3}}\alpha a_0^5 n_{\rm i} n_{\rm e}\langle Z^2 g_{\rm FF}\rangle\left(\frac{\chi_{\rm H}}{kT}\right)^{1/2}\left(\frac{\chi_{\rm H}}{h\nu}\right)^3 (1 - e^{-h\nu/kT}). \tag{42}$$

The BF opacity for a single element is written in similar terms. Here, only the H-like species population $n_{i,1}$ is relevant in the fully ionized limit, giving simply

$$\kappa_\nu^{\rm BF} = n_{i,1}\frac{64\pi}{3\sqrt{3}}\alpha a_0^2 \frac{Z^4}{p^5}\left(\frac{\chi_{\rm H}}{h\nu}\right)^3 (1 - e^{-h\nu/kT}) g_{i,\rm BF} \tag{43}$$

for the spectral range above the ionization edge. The BF opacity written in this way has strong hidden temperature and density dependence through $n_{i,1}$. The more-stationary product $n_{i,2}n_{\rm e}$ is substituted using the Saha equation [Eq. (40)] to obtain

$$\kappa_\nu^{\rm BF} = \frac{256\pi^{5/2}}{3\sqrt{3}}\alpha a_0^5 n_2 n_{\rm e}\left(\frac{\chi_{\rm H}}{kT}\right)^{3/2}\frac{g_1}{g_2}\frac{Z^4}{p^5}\left(\frac{\chi_{\rm H}}{h\nu}\right)^3 \times (1 - e^{-h\nu/kT}) e^{(\chi-\Delta\chi)/kT} g_{i,\rm BF}. \tag{44}$$

Again, considering a mixture of elements $i$, using $n_{i,2} \approx n_i$, we can write

$$\sum_i n_i Z_i^4 e^{(\chi-\Delta\chi)/kT} g_{i,\rm BF} = n_{\rm i}\langle Z^4 e^{(\chi-\Delta\chi)/kT} g_{\rm BF}\rangle, \tag{45}$$

giving

$$\kappa_\nu^{\rm BF} = \frac{256\pi^{5/2}}{3\sqrt{3}}\alpha a_0^5 n_{\rm i} n_{\rm e}\left(\frac{\chi_{\rm H}}{kT}\right)^{3/2}\frac{g_1}{g_2}\frac{1}{p^5}\left(\frac{\chi_{\rm H}}{h\nu}\right)^3 \times \langle Z^4 e^{(\chi-\Delta\chi)/kT} g_{\rm Z,BF}\rangle (1 - e^{-h\nu/kT}). \tag{46}$$

Applying the appropriate values for $g_1$, $g_2$, and $p$ given above for the H-like species, we have

$$\kappa_\nu^{\mathrm{BF}} = \frac{512\pi^{5/2}}{3\sqrt{3}}\alpha a_0^5 n_\mathrm{i} n_\mathrm{e}\left(\frac{\chi_\mathrm{H}}{kT}\right)^{3/2}\left(\frac{\chi_\mathrm{H}}{h\nu}\right)^3 \times \langle Z^4 e^{(\chi-\Delta\chi)/kT} g_{\mathrm{Z,BF}}\rangle(1-e^{-h\nu/kT}). \tag{47}$$

In LTE, the Kirchhoff relationship[17] $\varepsilon_\nu = \kappa_\nu B_\nu(T)$ is the statistical detailed-balance relationship between emissivity and opacity, or between any one absorption process and its time-inverse emission process. Therefore,

$$\frac{\varepsilon_\nu^{\mathrm{BF}}}{\varepsilon_\nu^{\mathrm{FF}}} = \frac{\kappa_\nu^{\mathrm{BF}}}{\kappa_\nu^{\mathrm{FF}}} \tag{48}$$

and, applying Eqs. (42) and (47),

$$\frac{\varepsilon_\nu^{\mathrm{BF}}}{\varepsilon_\nu^{\mathrm{FF}}} = \left(\frac{2\chi_\mathrm{H}}{kT}\right)\frac{\langle Z^4 e^{(\chi-\Delta\chi)/kT} g_{\mathrm{BF}}\rangle}{\langle Z^2 g_{\mathrm{FF}}\rangle}. \tag{49}$$

This ratio is independent of density, except at higher densities where continuum lowering $\Delta\chi \sim n_i^{1/3}$ becomes important. To gauge the relative importance of the participating processes, we set aside the Gaunt factors temporarily and write

$$\langle Z^4 e^{(\chi-\Delta\chi)/kT} g_{\mathrm{BF}}\rangle \approx \langle Z^4\rangle, \tag{50}$$

which is a valid simplification at very high temperatures, $kT \gg \chi \geq \chi_\mathrm{H}$, and

$$\langle Z^2 g_{\mathrm{FF}}\rangle \approx \langle Z^2\rangle. \tag{51}$$

It is easy to see from Eqs. (49)–(51) that we have been correct in neglecting FB emission in hydrogen, relative to FF emission, but that the $\langle Z^4\rangle/\langle Z^2\rangle$ charge scaling of the FB-to-FF ratio predicts significant FB emission from mid-$Z$ contaminants, in addition to their FF emission, even if they are present in trace amounts relative to hydrogen.

It may appear paradoxical that the BF-to-FF ratio given by Eq. (49) is independent of density, considering that BF absorption is initiated by a two-body (photon–ion) interaction, implying that its opacity is linear in density, while FF absorption is initiated by a three-body (photon–electron–ion) interaction, implying that its opacity is second order in density. In general, the ratio of densities in the BF-to-FF opacity ratio is density dependent, but since we are working in the near-complete ionization regime where all the bound-electron species are H-like, the Saha equation [Eq. (40)] removes this density dependence.

The Planck function in the Kirchhoff relationship can be written as

$$B_\nu(T) = \frac{\chi_\mathrm{H}\alpha^2\left(\frac{h\nu}{\chi_\mathrm{H}}\right)^3}{8\pi^2 a_0^2}\frac{1}{e^{h\nu/kT}-1}. \tag{52}$$

The individual emissivity contributions are, then

$$\varepsilon_\nu^{\mathrm{FF}} = \frac{32}{3}\sqrt{\frac{\pi}{3}}\alpha^3\chi_\mathrm{H} a_0^3 n_\mathrm{i} n_\mathrm{e}\langle Z^2 g_{\mathrm{FF}}\rangle\left(\frac{\chi_\mathrm{H}}{kT}\right)^{1/2} e^{-h\nu/kT}, \tag{53}$$

repeating Eq. (8), and

$$\varepsilon_\nu^{\mathrm{BF}} = \frac{64}{3}\sqrt{\frac{\pi}{3}}\alpha^3\chi_\mathrm{H} a_0^3 n_\mathrm{i} n_\mathrm{e}\left(\frac{\chi_\mathrm{H}}{kT}\right)^{3/2}\langle Z^4 e^{(\chi-\Delta\chi)/kT} g_{\mathrm{BF}}\rangle e^{-h\nu/kT}, \tag{54}$$

with a total emissivity

$$\varepsilon_\nu = \frac{32}{3}\sqrt{\frac{\pi}{3}}\alpha^3\chi_\mathrm{H} a_0{}^3 n_\mathrm{i} n_\mathrm{e}\left(\frac{\chi_\mathrm{H}}{kT}\right)^{1/2} \times\left[\langle Z^2 g_{\mathrm{FF}}\rangle + 2\left(\frac{\chi_\mathrm{H}}{kT}\right)\langle Z^4 e^{(\chi-\Delta\chi)/kT} g_{\mathrm{BF}}\rangle\right] e^{-h\nu/kT}. \tag{55}$$

This expression can be evaluated to obtain the enhancement of the photon yield resulting from the increase in both $\langle Z^2 g_{\mathrm{FF}}\rangle$ and $\langle Z^4 e^{(\chi-\Delta\chi)/kT} g_{\mathrm{BF}}\rangle$ from CH shell–mix contamination. Formally, CH mix reduces the neutron yield through the $\mathrm{n_D n_T}$ product of fuel ion densities in Eq. (30), which is only minutely affected by a trace contamination. Equation (30) itself, then, need not be altered in any way.

As was noted in Sec. II, the Kulsrud Gaunt factor for hydrogen differs only slightly from the more reliable KL values for hydrogen in our relevant temperature range, but it is not applicable to carbon under ICF hot-spot conditions or to FB emission. Power-law fits to KL results have been obtained near $h\nu_0 \approx 5.39$ keV and $h\nu_0/kT \approx 2$ for the Gaunt factors needed to evaluate Eq. (55) (Ref. 22). These are

$$g_{\mathrm{H,FF}} \approx 0.966(h\nu/kT)^{-0.41},\ g_{\mathrm{H,FB}} \approx 0.299(h\nu/5.39\mathrm{keV})^{-0.430},$$
$$g_{\mathrm{C,FF}} \approx 1.28(h\nu/kT)^{-0.23},\ g_{\mathrm{C,FB}} \approx 0.926(h\nu/5.39\mathrm{keV})^{-0.141}. \tag{56}$$

The FF Gaunt factors depend on temperature because the FF absorption cross section is an average over the Maxell–Boltzmann distribution of initial free-electron states. The FB Gaunt factor, on the other hand, does not depend on temperature because all properties of the single-electron bound states are attributes of the ion, not the free-electron plasma. We find that adding a fraction $f_{\mathrm{CH}} = 2.4\%$ by atom of CH to a pure hydrogen core, as in the uniform mix of shell polymer into the hot spot, doubles the emissivity at $h\nu_0 \approx 5.39$ keV. This represents a mix mass of $\Delta M_{\mathrm{CH}} = 125$ ng in the example described in Sec. II, where the hot-spot mass is $M_{\mathrm{HS}} = 2.1\ \mu$g, which happens to be the mean hot-spot mass of the entire ensemble of simulations analyzed in Sec. IV. The standard deviation of hot-spot masses in this ensemble is only 17%, so the emission-doubling mix mass is roughly the same for all the implosions. The measured emission enhancements of the low-adiabat implosions plotted in Fig. 11 range over factors from 2 to 3, which correspond to a range of mix mass from 125 ng to 250 ng. The enhancement factor corresponding to a 2.4%-by-atom contamination level is shown plotted as the black (blue online) curve in Fig. 12 as a function of temperature. Within the range of plausible hot-spot temperatures indicated by the blue-shaded region, $2\,\mathrm{keV} < kT < 3\,\mathrm{keV}$, the enhancement factor is a weak function of temperature, primarily the result of the temperature dependences of the relevant Gaunt factors listed in Eq. (56).

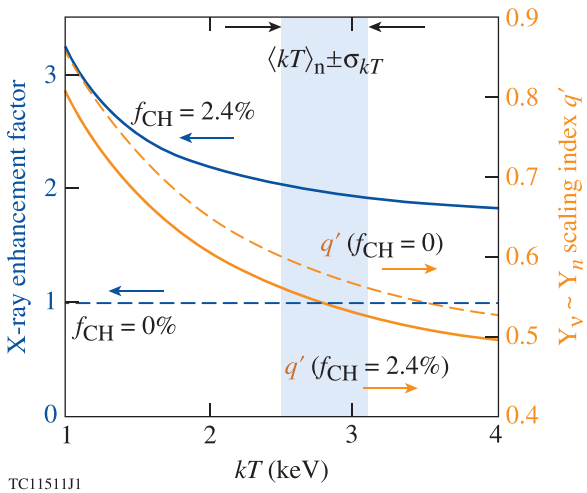


FIG. 12. Photon-yield enhancement resulting from a 2.4% CH, by atom, contamination of the hot spot, as a function of temperature. The photon emissivity of a hot spot is expected to double when contaminated at this level. This enhancement factor varies with hot-spot temperature, as shown by the black (blue) from the left axis. The light gray (blue) shaded band emphasizes the range of temperature within one standard deviation of the simulation ensemble mean neutron-averaged hot-spot temperature. The solid gray (orange) curve from the right axis shows the modified scaling index $q'$ of the yield quotient $Y_{\nu_0}/Y_n^{q'}$ as a function of temperature, and the dashed (orange) curve shows the original zero-mix scaling index for comparison. The black (blue) horizontal dashed line shows the enhancement level (unity) corresponding to zero contamination.

The yield-ratio scaling index $q$, plotted as the solid gray (orange online) curve, varies with temperature in the contaminated core, as it does in the pure hydrogen core in Fig. 10, plotted here as the dashed gray (orange online) curve. The small difference between these two curves is accounted for by the Gaunt factors for the FB emission, which accounts for very roughly half the emission in Fig. 12 and none of the emission in Fig. 10, does not depend on temperature. The dashed black (blue online) line shows the enhancement factor (unity) corresponding to zero contamination.

The additional radiative cooling from a trace concentration of CH mix may lower the temperature of the hot spot and reduce the neutron yield. The effects of a modest temperature drop on the yield scaling, the x-ray yield normalization, and the x-ray yield mix enhancement are shown in Figs. 10 and 12, where it is seen that they will most likely be small. The only one of the equations leading to these results that is potentially affected by hot-spot cooling is Eq. (24), which is obtained from the balance of inner-shell ablation into the hot spot and thermal conduction loss out of the hot spot into the shell that establishes an adiabatic hot-spot volume. This equation was derived by neglecting radiation losses from the uncontaminated hot spot, and we continue to assume that this approximation is valid if the radiation losses are increased by only a modest factor by a trace contamination by CH. The other equations used to obtain the photon-neutron yield scaling are not affected by radiation. The effect of mix on the photon-neutron yield scaling enters our analysis through the $Z$-dependent terms in Eq. (55). Figure 12, however, shows that the nominal 2.4% contamination has a reasonably small effect on the photon-neutron yield scaling parameter. We may, then, use the same yield normalization for clean and contaminated hot spots, and the normalized photon yield will be affected relatively little, other than by a factor that depends almost exclusively on the CH contamination concentration. This is the enhancement factor shown in Fig. 12 for the case of 2.4% CH contamination.

To estimate the importance of hot-spot radiation cooling, we begin with a conservative estimate of the emission time of an uncontaminated hot spot at stagnation

$$\tau_{\rm rad} = -E/\dot{E}, \tag{57}$$

where

$$E = \frac{3}{2}P \tag{58}$$

is the thermal energy density and where

$$\dot{E} = -\int_0^\infty \varepsilon_\nu^{\rm FF}\,{\rm d}\nu \tag{59}$$

is the integrated emission per volume, assuming free escape over the entire spectrum. The emissivity $\varepsilon_\nu^{\rm FF}$ given by Eq. (13) can be used. The result

$$\tau_{\rm rad} \approx 1.25\,\frac{(kT/2.8\,{\rm keV})^{3/2}}{(P/87.6\,{\rm Gbar})}\,{\rm ns} \tag{60}$$

is expressed showing the temperature and pressure scaling in units of 2.8 keV and 87.6 Gbar, respectively, which are the average values from our simulation ensemble. This cooling time of 1.25 ns is an order of magnitude larger than the stagnation time or hot-spot lifetime of 79 ps, which is the ensemble-average neutron burnwidth value, indicating that uncontaminated hot spots will emit no more than one tenth of their thermal energy during stagnation. In the simulation ensemble, the radiation loss fraction is closer to roughly $\sim$0.15. Figure 11 shows that a doubling of the normalized emission is typical, suggesting that about a third of the hot-spot energy may be radiated away, which is considerable. Nevertheless, examining Fig. 12 shows that the doubling effect of a 2.4% contamination at a temperature near 3 keV is still close to a doubling effect at 2 keV and that the drop in the scaling index caused by a 2.4% contamination at a temperature near 3 keV is substantially reversed as the temperature approaches 2 keV. Our reliance on an adiabatic hot spot through Eq. (24), then, may not be a quantitatively reliable assumption for more than a trace CH mix concentration, but we claim that it is adequate for our immediate purpose of obtaining first estimates of hot-spot mix masses.

A set of similar mix-mass measurements has been reported for cryogenic implosions on the NIF based on the ratio of the x-ray and neutron yields.[14] To describe this technique in terms of the discussion above, we write Eq. (28) once again, but with the mix effect included as in Eq. (55)

$$Y_{\nu_0} \propto P^2 \frac{e^{-h\nu/kT}}{T^{2-\eta}} \left(\frac{\chi_{\rm H}}{kT}\right)^{1/2} (1+\langle Z\rangle) \times \left[\langle Z^2 g_{\rm FF}\rangle + 2\left(\frac{\chi_{\rm H}}{kT}\right)\langle Z^4 e^{(\chi-\Delta\chi)/kT} g_{\rm BF}\rangle\right] V\Delta t. \tag{61}$$

Our discussion parallels the discussion in Ref. 14 to some extent, although the mix-mass estimates presented in Ref. 14 are based ultimately on emissivity values obtained from detailed atomic calculations, rather than the Kramers–Gaunt formulation underlying Eq. (61). The ratio of the photon to neutron yield can be constructed from Eq. (30) and Eq. (61) with the result being

$$\frac{Y_{\nu_0}}{Y_n} \propto \frac{e^{-h\nu/kT}}{T^{4+\varepsilon-\eta}} \left(\frac{\chi_{\rm H}}{kT}\right)^{1/2} (1+\langle Z\rangle) \times \left[\langle Z^2 g_{\rm FF}\rangle + 2\left(\frac{\chi_{\rm H}}{kT}\right)\langle Z^4 e^{(\chi-\Delta\chi)/kT} g_{\rm BF}\rangle\right] \tag{62}$$

to within fixed constants. This is the quantity that was measured in the NIF experiments. In forming this ratio, the pressure factors, the hot-spot volumes, and the emission times cancel. It was assumed here as well that the temperature and neutron emission rate were spatially uniform, that the electron and ion temperatures were equal, and that the photon and neutron emission volumes and times were equal. Since OMEGA and non-igniting NIF implosions stagnate in comparable temperature ranges, we can examine this yield ratio in an approximate fashion by allowing $\eta = \varepsilon = 0$, and applying the Kulsrud limit $g_{\rm FF} \propto T^{0.5}$ for both hydrogen and carbon and the same temperature independence for $g_{\rm FB}$, which is a better approximation near $h\nu_0 = 10.85$ keV used in the NIF measurements than near $h\nu_0 = 5.30$ keV used in the OMEGA experiments. This gives

$$\frac{Y_{\nu_0}}{Y_{\rm n}} \propto \frac{e^{-h\nu/kT}}{T^4}(1+\langle Z\rangle)\left[\langle Z^2\rangle + 2\left(\frac{\chi_{\rm H}}{kT}\right)\frac{g_{\rm BF}}{g_{\rm FF}}\langle Z^4\rangle\right]. \tag{63}$$

The argument supporting the mix-mass estimates based on measurements of this yield ratio in the NIF experiments is that, according to an equation very much like Eq. (63), the yield ratio is related directly to the charge averages, and consequently to the mix atomic fractions

$$\langle Z^n\rangle = 1 + (6^n - 1)\frac{f_{\rm CH}}{2}. \tag{64}$$

Since the hydrogen and carbon are nearly fully ionized, the ion charges are effectively fixed, and everything else is a weak function of temperature.[14] Based on the condition given by Eq. (19) for $n = 4$, the leading factor of Eq. (63) is independent of temperature for a range of temperatures centered at $kT_0 = h\nu_0/4$ or $kT_0 = 2.71$ keV, which is almost exactly the center of the range of temperatures, $1.7\,\text{keV} < kT < 3.9\,\text{keV}$ given in Ref. 14 as the range of applicable source temperatures. These NIF mix-mass measurements are another example of how making x-ray measurements at an appropriate spectral energy simplifies their analysis in a very important way.

The contamination fractions measured on OMEGA at the level of $f_{\rm CH} = 2.4\%$ to 4.8% are similar to the range of mix fractions measured on the NIF.[14] Given the obvious dissimilarities between NIF indirect-drive implosions driven by two orders of magnitude more laser energy than the OMEGA direct-drive implosions, the similar mix fractions become an interesting point of comparison for future consideration. A few remarks will suffice for now. We note that the NIF capsules are roughly twice the diameter of the OMEGA capsules.[38] Assuming naively that all characteristic lengths and times of an implosion scale in direct proportion to the initial capsule radius, i.e., if the experiments on the two platforms were self-similar versions of each other, then the material composition profiles should be self-similar as well. Comparable mix fractions would result from shell perturbation amplitudes growing to comparable fractions of the capsule radius. For spherical-harmonic perturbation modes of the same harmonic order, the perturbation wavelengths scale with radius. The saturation amplitude, which is the point where linear perturbation growth transitions to nonlinear growth and, perhaps, turbulent mix, occurs at a specific ratio of amplitude to wavelength.[39] Since both the wavelengths and the amplitudes scale in direct proportion to the capsule radius, the transition to turbulence should be self-similar in both series of implosions. No doubt, this self-similarity does not apply to all aspects of an implosion.[4] If mix is regarded as a surface phenomenon, comparable mix masses per volume indicate roughly twice the mix mass per shell area in the NIF capsules than in the OMEGA targets since the former have roughly twice the volume-to-surface-area ratio as the latter. These tentative remarks do not identify which series of implosions was more unstable or which of the two mix fractions is larger, relative to expected performance, but it is clear that mix measurements are now possible and experimental progress in addressing these and other questions can be expected in the future.

## VI. CONCLUSIONS

The scaling behavior of the x-ray emissivity of hydrogen hot spots in ICF implosions has been examined. Using the pressure- and temperature-dependence of x-ray continuum emission, we have shown that the pressure can be inferred from the emissivity measured within a specific spectral energy range without requiring accurate prior knowledge of the source temperature. This is significant because the pressure is a key parameter characterizing an isobaric hot spot;[8] it is a measure of the scaled-equivalent ignition performance of an implosion; and it is an example of a quantity that can be measured in direct or advantageous ways with spectral responses that have been optimized to the task.

The scaling relationship between the photon and neutron yields of OMEGA cryogenic implosions that has been observed in simulation results and used to isolate excess x-ray emission from low-adiabat implosions has been explained. We have brought together x-ray emission and neutron yield scaling results to produce the first estimates of the fuel–shell mix mass in OMEGA implosions. The scaling properties of both the x-ray emissivity at the chosen spectral energy and the neutron yield allow one to normalize the x-ray emission with respect to the scaled neutron yield so that excess normalized emission becomes a measure of the CH polymer mass from the shell that has mixed into the hot spot during the implosion, up to the time of stagnation. It is a matter of some interest that this neutron–photon scaling,

which has gone unexplained in the past, is now understood. It is of particular interest to the progress of cryogenic implosion research on the OMEGA Laser System that we have estimates of the mix mass. In a number of important respects, this approach to mix-mass estimation is similar to that of the x-ray continuum-based mix-mass measurements on the NIF. It is interesting that both sets of measurements describe similar levels of mix contamination, and the implications of this will be interesting to consider in the future.

## ACKNOWLEDGMENTS

This material was based upon work supported by the Department of Energy National Nuclear Security Administration under Award No. DE-NA0001944, the University of Rochester, the New York State Energy Research and Development Authority, and the Office of Fusion Energy Sciences No. DE-FG02-04ER54786. The support of DOE does not constitute an endorsement by DOE of the views expressed in this article.

[1]J. Nuckolls, L. Wood, A. Thiessen, and G. Zimmerman, Nature **239**, 139 (1972).

[2]J. D. Lindl, Phys. Plasmas **2**, 3933 (1995); J. D. Lindl, P. Amendt, R. L. Berger, S. G. Glendinning, S. H. Glenzer, S. W. Haan, R. L. Kauffman, O. L. Landen, and L. J. Suter, *ibid.* **11**, 339 (2004).

[3]S. Atzeni and J. Meyer-ter-Vehn, *The Physics of Inertial Fusion: Beam Plasma Interaction, Hydrodynamics, Hot Dense Matter*, International Series of Monographs on Physics (Clarendon Press, Oxford, 2004).

[4]R. Nora, R. Betti, K. S. Anderson, A. Shvydky, A. Bose, K. M. Woo, A. R. Christopherson, J. A. Marozas, T. J. B. Collins, P. B. Radha, S. X. Hu, R. Epstein, F. J. Marshall, R. L. McCrory, T. C. Sangster, and D. D. Meyerhofer, Phys. Plasmas **21**, 056316 (2014).

[5]V. N. Goncharov, T. C. Sangster, R. Betti, T. R. Boehly, M. J. Bonino, T. J. B. Collins, R. S. Craxton, J. A. Delettrez, D. H. Edgell, R. Epstein, R. K. Follet, C. J. Forrest, D. H. Froula, V. Yu. Glebov, D. R. Harding, R. J. Henchen, S. X. Hu, I. V. Igumenshchev, R. Janezic, J. H. Kelly, T. J. Kessler, T. Z. Kosc, S. J. Loucks, J. A. Marozas, F. J. Marshall, A. V. Maximov, R. L. McCrory, P. W. McKenty, D. D. Meyerhofer, D. T. Michel, J. F. Myatt, R. Nora, P. B. Radha, S. P. Regan, W. Seka, W. T. Shmayda, R. W. Short, A. Shvydky, S. Skupsky, C. Stoeckl, B. Yaakobi, J. A. Frenje, M. Gatu-Johnson, R. D. Petrasso, and D. T. Casey, Phys. Plasmas **21**, 056315 (2014).

[6]P. T. Springer, C. Cerjan, R. Betti, J. A. Caggiano, M. J. Edwards, J. A. Frenje, V. Yu. Glebov, S. H. Glenzer, S. M. Glenn, N. Izumi, O. Jones, G. Kyrala, T. Ma, J. McNaney, M. Moran, D. H. Munro, S. Regan, T. C. Sangster, S. Sepke, H. Scott, R. P. J. Town, S. V. Weber, and B. Wilson, EPJ Web Conf. **59**, 04001 (2013); C. Cerjan, P. T. Springer, and S. M. Sepke, Phys. Plasmas **20**, 056319 (2013).

[7]J. D. Lawson, Proc. Phys. Soc. London, B **70**, 6 (1957).

[8]R. Betti, P. Y. Chang, B. K. Spears, K. S. Anderson, J. Edwards, M. Fatenejad, J. D. Lindl, R. L. McCrory, R. Nora, and D. Shvarts, Phys. Plasmas **17**, 058102 (2010); S. H. Glenzer, D. A. Callahan, A. J. MacKinnon, J. L. Kline, G. Grim, E. T. Alger, R. L. Berger, L. A. Bernstein, R. Betti, D. L. Bleuel, T. R. Boehly, D. K. Bradley, S. C. Burkhart, R. Burr, J. A. Caggiano, C. Castro, D. T. Casey, C. Choate, D. S. Clark, P. Celliers, C. J. Cerjan, G. W. Collins, E. L. Dewald, P. DiNicola, J. M. DiNicola, L. Divol, S. Dixit, T. Döppner, R. Dylla-Spears, E. Dzenitis, M. Eckart, G. Erbert, D. Farley, J. Fair, D. Fittinghoff, M. Frank, L. J. A. Frenje, S. Friedrich, M. Gatu Johnson, C. Gibson, E. Giraldez, V. Glebov, S. Glenn, N. Guler, S. W. Haan, B. J. Haid, B. A. Hammel, A. V. Hamza, C. A. Haynam, G. M. Heestand, M. Hermann, H. W. Hermann, D. G. Hicks, D. E. Hinkel, J. P. Holder, D. M. Holunda, J. B. Horner, W. W. Hsing, H. Huang, N. Izumi, M. Jackson, O. S. Jones, D. H. Kalantar, R. Kauffman, J. D. Kilkenny, R. K. Kirkwood, J. Klingmann, T. Kohut, J. P. Knauer, J. A. Koch, B. Kozioziemki, G. A. Kyrala, A. L. Kritcher, J. Kroll, K. La Fortune, L. Lagin, O. L. Landen, D. W. Larson, D. LaTray, R. J. Leeper, S. Le Pape, J. D. Lindl, R. Lowe-Webb, T. Ma, J. McNaney, A. G. MacPhee, T. N. Malsbury, E. Mapoles, C. D. Marshall, N. B. Meezan, F. Merrill, P. Michel, J. D. Moody, A. S. Moore, M. Moran, K. A. Moreno, D. H. Munro, B. R. Nathan, A. Nikroo, R. E. Olson, C. D. Orth, A. E. Pak, P. K. Patel, T. Parham, R. Petrasso, J. E. Ralph, H. Rinderknecht, S. P. Regan, H. F. Robey, J. S. Ross, M. D. Rosen, R. Sacks, J. D. Salmonson, R. Saunders, J. Sater, C. Sangster, M. B. Schneider, F. H. Séguin, M. J. Shaw, B. K. Spears, P. T. Springer, W. Stoeffl, L. J. Suter, C. A. Thomas, R. Tommasini, R. P. J. Town, C. Walters, S. Weaver, S. V. Weber, P. J. Wegner, P. K. Whitman, K. Widmann, C. C. Widmayer, C. H. Wilde, D. C. Wilson, B. Van Wonterghem, B. J. MacGowan, L. J. Atherton, M. J. Edwards, and E. I. Moses, *ibid.* **19**, 056318 (2012).

[9]T. R. Boehly, D. L. Brown, R. S. Craxton, R. L. Keck, J. P. Knauer, J. H. Kelly, T. J. Kessler, S. A. Kumpan, S. J. Loucks, S. A. Letzring, F. J. Marshall, R. L. McCrory, S. F. B. Morse, W. Seka, J. M. Soures, and C. P. Verdon, Opt. Commun. **133**, 495 (1997).

[10]H. R. Griem, *Principles of Plasma Spectroscopy* (Cambridge University Press, Cambridge, England, 1997).

[11]S. Yu. Gus'kov, O. N. Krokhin, and V. B. Rozanov, Nucl. Fusion **16**, 957 (1976).

[12]R. Betti, M. Umansky, V. Lobatchev, V. N. Goncharov, and R. L. McCrory, Phys. Plasmas **8**, 5257 (2001).

[13]W. J. Hogan, E. I. Moses, B. E. Warner, M. S. Sorem, and J. M. Soures, Nucl. Fusion **41**, 567 (2001); G. H. Miller, E. I. Moses, and C. R. Wuest, Opt. Eng. **43**, 2841 (2004); S. H. Glenzer, B. K. Spears, M. J. Edwards, E. T. Alger, R. L. Berger, D. L. Bleuel, D. K. Bradley, J. A. Caggiano, D. A. Callahan, C. Castro, D. T. Casey, C. Choate, D. S. Clark, C. J. Cerjan, G. W. Collins, E. L. Dewald, J.-M. G. Di Nicola, P. Di Nicola, L. Divol, S. N. Dixit, T. Döppner, R. Dylla-Spears, E. G. Dzenitis, J. E. Fair, L. J. A. Frenje, M. Gatu Johnson, E. Giraldez, V. Glebov, S. M. Glenn, S. W. Haan, B. A. Hammel, S. P. Hatchett II, C. A. Haynam, R. F. Heeter, G. M. Heestand, H. W. Herrmann, D. G. Hicks, D. M. Holunga, J. B. Horner, H. Huang, N. Izumi, O. S. Jones, D. H. Kalantar, J. D. Kilkenny, R. K. Kirkwood, J. L. Kline, J. P. Knauer, B. Kozioziemski, A. L. Kritcher, J. J. Kroll, G. A. Kyrala, K. N. LaFortune, O. L. Landen, D. W. Larson, R. J. Leeper, S. Le Pape, J. D. Lindl, T. Ma, A. J. Mackinnon, A. G. MacPhee, E. Mapoles, P. W. McKenty, N. B. Meezan, P. Michel, J. L. Milovich, J. D. Moody, A. S. Moore, M. Moran, K. A. Moreno, D. H. Munro, B. R. Nathan, A. Nikroo, R. E. Olson, C. D. Orth, A. Pak, P. K. Patel, T. Parham, R. Petrasso, J. E. Ralph, H. Rinderknecht, S. P. Regan, H. F. Robey, J. S. Ross, J. D. Salmonson, C. Sangster, J. Sater, M. B. Schneider, F. H. Séguin, M. J. Shaw, M. J. Shoup, P. T. Springer, W. Stoeffl, L. J. Suter, C. A. Thomas, R. P. J. Town, C. Walters, S. V. Weber, P. J. Wegner, C. Widmayer, P. K. Whitman, K. Widmann, D. C. Wilson, B. M. Van Wonterghem, B. J. MacGowan, L. J. Atherton, and E. I. Moses, Plasma Phys. Control. Fusion **54**, 045013 (2012).

[14]T. Ma, P. K. Patel, N. Izumi, P. T. Springer, M. H. Key, L. J. Atherton, L. R. Benedetti, D. K. Bradley, D. A. Callahan, P. M. Celliers, C. J. Cerjan, D. S. Clark, E. L. Dewald, S. N. Dixit, T. Döppner, D. H. Edgell, R. Epstein, S. Glenn, G. Grim, S. W. Haan, B. A. Hammel, D. Hicks, W. W. Hsing, O. S. Jones, S. F. Khan, J. D. Kilkenny, J. L. Kline, G. A. Kyrala, O. L. Landen, S. Le Pape, B. J. MacGowan, A. J. Mackinnon, A. G. MacPhee, N. B. Meezan, J. D. Moody, A. Pak, T. Parham, H.-S. Park, J. E. Ralph, S. P. Regan, B. A. Remington, H. F. Robey, J. S. Ross, B. K. Spears, V. Smalyuk, L. J. Suter, R. Tommasini, R. P. Town, S. V. Weber, J. D. Lindl, M. J. Edwards, S. H. Glenzer, and E. I. Moses, Phys. Rev. Lett. **111**, 085004 (2013).

[15]S. P. Regan, R. Epstein, B. A. Hammel, L. J. Suter, J. Ralph, H. Scott, M. A. Barrios, D. K. Bradley, D. A. Callahan, C. Cerjan, G. W. Collins, S. N. Dixit, T. Doeppner, M. J. Edwards, D. R. Farley, S. Glenn, S. H. Glenzer, I. E. Golovkin, S. W. Haan, A. Hamza, D. G. Hicks, N. Izumi, J. D. Kilkenny, J. L. Kline, G. A. Kyrala, O. L. Landen, T. Ma, J. J. MacFarlane, R. C. Mancini, R. L. McCrory, N. B. Meezan, D. D. Meyerhofer, A. Nikroo, K. J. Peterson, T. C. Sangster, P. Springer, and R. P. J. Town, Phys. Plasmas **19**, 056307 (2012); S. P. Regan, R. Epstein, B. A. Hammel, L. J. Suter, H. A. Scott, M. A. Barrios, D. K. Bradley, D. A. Callahan, C. Cerjan, G. W. Collins, S. N. Dixit, T. Döppner, M. J. Edwards, D. R. Farley, K. B. Fournier, S. Glenn, S. H. Glenzer, I. E. Golovkin, S. W. Haan, A. Hamza, D. G. Hicks, N. Izumi, O. S. Jones, J. D. Kilkenny, J. L. Kline, G. A. Kyrala, O. L. Landen, T. Ma, J. J. MacFarlane, A. J. MacKinnon, R. C. Mancini, R. L. McCrory, N. B. Meezan, D. D. Meyerhofer, A. Nikroo, H.-S. Park, J. Ralph, B. A. Remington, T. C. Sangster, V. A. Smalyuk, P. T. Springer, and R. P. J. Town, Phys. Rev. Lett. **111**, 045001 (2013).

[16]B. A. Hammel, H. A. Scott, S. P. Regan, C. Cerjan, D. S. Clark, M. J. Edwards, R. Epstein, S. H. Glenzer, S. W. Haan, N. Izumi, J. A. Koch, G. A. Kyrala, O. L. Landen, S. H. Langer, K. Peterson, V. A. Smalyuk, L. J. Suter, and D. C. Wilson, Phys. Plasmas **18**, 056310 (2011).
[17]S. Chandrasekhar, *Radiative Transfer* (Dover Publications, New York, 1960).
[18]R. N. Bracewell, *The Fourier Transform and Its Applications*, 3rd ed. (McGraw-Hill, Boston, 2000).
[19]H. A. Kramers, Philos. Mag. **46**, 836 (1923).
[20]J. A. Gaunt, Proc. R. Soc. London, A **126**, 654 (1930).
[21]A. Messiah, *Quantum Mechanics* (North-Holland, Amsterdam, 1966),Vol. II, p. 664 ff.
[22]W. J. Karzas and R. Latter, Astrophys. J. Suppl. Ser. **6**, 167 (1961).
[23]M. Nakagawa, Y. Kohyama, and N. Itoh, Astrophys. J. Suppl. Ser. **63**, 661 (1987).
[24]F. Perrot, Laser Part. Beams **14**, 731 (1996); V. N. Tsytovich, R. Bingham, U. de Angelis, and A. Forlani, J. Quant. Spectrosc. Radiat. Transfer **57**, 241 (1997).
[25]A. N. Cox, in *Stars and Stellar Systems*, edited by L. H. Aller and D. B. McLaughlin, Stellar Structure, Vol. VIII (The University of Chicago Press, Chicago, 1965), p. 195.
[26]B. F. Rozsnyai, Phys. Rev. A **43**, 3035 (1991); S. Mazevet, L. A. Collins, N. H. Magee, J. D. Kress, and J. J. Keady, Astron. Astrophys. **405**, L5 (2003).
[27]S. X. Hu, L. A. Collins, V. N. Goncharov, T. R. Boehly, R. Epstein, R. L. McCrory, and S. Skupsky, Phys. Rev. E **90**, 033111 (2014).
[28]R. M. Kulsrud, Astrophys. J. **119**, 386 (1954).
[29]F. J. Marshall and J. A. Oertel, Rev. Sci. Instrum. **68**, 735 (1997).
[30]T. C. Sangster, V. N. Goncharov, R. Betti, P. B. Radha, T. R. Boehly, D. T. Casey, T. J. B. Collins, R. S. Craxton, J. A. Delettrez, D. H. Edgell, R. Epstein, C. J. Forrest, J. A. Frenje, D. H. Froula, M. Gatu-Johnson, V. Yu. Glebov, D. R. Harding, M. Hohenberger, S. X. Hu, I. V. Igumenshchev, R. Janezic, J. H. Kelly, T. J. Kessler, C. Kingsley, T. Z. Kosc, J. P. Knauer, S. J. Loucks, J. A. Marozas, F. J. Marshall, A. V. Maximov, R. L. McCrory, P. W. McKenty, D. D. Meyerhofer, D. T. Michel, J. F. Myatt, R. D. Petrasso, S. P. Regan, W. Seka, W. T. Shmayda, R. W. Short, A. Shvydky, S. Skupsky, J. M. Soures, C. Stoeckl, W. Theobald, V. Versteeg, B. Yaakobi, and J. D. Zuegel, Phys. Plasmas **20**, 056317 (2013).
[31]J. Delettrez, R. Epstein, M. C. Richardson, P. A. Jaanimagi, and B. L. Henke, Phys. Rev. A **36**, 3926 (1987).
[32]J. J. MacFarlane, I. E. Golovkin, P. Wang, P. R. Woodruff, and N. A. Pereyra, High Energy Density Phys. **3**, 181 (2007); Prism Computational Sciences, Inc., Madison, WI 53711.
[33]G. A. Kyrala, S. Dixit, S. Glenzer, D. Kalantar, D. Bradley, N. Izumi, N. Meezan, O. L. Landen, D. Callahan, S. V. Weber, J. P. Holder, S. Glenn, M. J. Edwards, P. Bell, J. Kimbrough, J. Koch, R. Prasad, L. Suter, J. L. Kline, and J. Kilkenny, Rev. Sci. Instrum. **81**, 10E316 (2010); M. A. Barrios, S. P. Regan, L. J. Suter, S. Glenn, L. R. Benedetti, D. K. Bradley, G. W. Collins, R. Epstein, B. A. Hammel, G. A. Kyrala, N. Izumi, T. Ma, H. Scott, and V. A. Smalyuk, Phys. Plasmas **20**, 072706 (2013).
[34]H.-S. Bosch and G. M. Hale, Nucl. Fusion **32**, 611 (1992).
[35]C. D. Zhou and R. Betti, Phys. Plasmas **14**, 072703 (2007).
[36]L. Rayleigh, Proc. London Math Soc. **XIV**, 170 (1883); G. Taylor, Proc. R. Soc. London Ser. A **201**, 192 (1950); S. Chandrasekhar, in *Hydrodynamic and Hydromagnetic Stability*, International Series of Monographs on Physics (Clarendon Press, Oxford, 1961).
[37]J. C. Stewart and K. D. Pyatt, Jr., Astrophys. J. **144**, 1203 (1966).
[38]S. W. Haan, J. D. Lindl, D. A. Callahan, D. S. Clark, J. D. Salmonson, B. A. Hammel, L. J. Atherton, R. C. Cook, M. J. Edwards, S. Glenzer, A. V. Hamza, S. P. Hatchett, M. C. Herrmann, D. E. Hinkel, D. D. Ho, H. Huang, O. S. Jones, J. Kline, G. Kyrala, O. L. Landen, B. J. MacGowan, M. M. Marinak, D. D. Meyerhofer, J. L. Milovich, K. A. Moreno, E. I. Moses, D. H. Munro, A. Nikroo, R. E. Olson, K. Peterson, S. M. Pollaine, J. E. Ralph, H. F. Robey, B. K. Spears, P. T. Springer, L. J. Suter, C. A. Thomas, R. P. Town, R. Vesey, S. V. Weber, H. L. Wilkens, and D. C. Wilson, Phys. Plasmas **18**, 051001 (2011).
[39]S. W. Haan, Phys. Fluids B **3**, 2349 (1991).